Article

Geochemical Features of Ground Ice from the Faddeevsky Peninsula Eastern Coast (Kotelny Island, East Siberian Arctic) as a Key to Understand Paleoenvironmental Conditions of Its Formation

Anfisa Pismeniuk [1,2,*], Petr Semenov [2], Alexandra Veremeeva [3], Wei He [4], Anna Kozachek [5], Sergei Malyshev [2], Elizaveta Shatrova [2], Anastasiia Lodochnikova [2] and Irina Streletskaya [1]

1   Department of Cryolitology and Glaciology, Faculty of Geography, Lomonosov Moscow State University, 119991 Moscow, Russia
2   All-Russia Institute of Geology and Mineral Resources of the World Ocean (VNIIOkeangeologia), 190121 Saint Petersburg, Russia
3   Institute of Physicochemical and Biological Problems in Soil Science, Russian Academy of Sciences, 142290 Pushchino, Russia
4   School of Water Resources and Environment, China University of Geoscience Beijing, Beijing 100083, China
5   Climate and Environmental Research Laboratory, Arctic and Antarctic Research Institute, 199397 Saint Petersburg, Russia
*   Correspondence: apismeniuk@geogr.msu.ru

Abstract: Understanding paleoenvironmental conditions of the permafrost formation allows us to estimate the permafrost carbon pool and its behavior upon thawing in a changing climate. In order to classify different types of ground ice and to reconstruct paleoenvironments, we examined geochemical data of ice wedges (IWs), tabular ground ice (TGI), and lens ice from the eastern coast of the Faddeevsky Peninsula (East Siberian Arctic). We analyzed isotope and ion composition, molecular composition of the gas phase, bulk biogeochemical parameters and dissolved organic matter (DOM) composition in ground ice samples. IWs formed in the Late Pleistocene under the coldest winter conditions and in the Holocene in proximity to the sea. The Holocene IWs have the highest mean d-excess (11–13‰) and a heavier isotope composition by an average of 6‰ compared with the Late Pleistocene IWs. We observe predominance of sea-salt fractions in ion composition of the Holocene IWs, while the Late Pleistocene IW shows enrichment in non-sea-salt component of SO_4^{2-} ($nssSO_4^{2-}$), which is probably associated with mineral leaching of deposits. Higher dissolved organic carbon (DOC) content in the Late Pleistocene IW (to 17.7 mg/L) may indicate more favorable vegetation conditions or lower degree of organic matter mineralization compared to Holocene IWs and TGI. CH_4 concentrations were relatively low with a maximum value of 2.27 μmol/L. DOM composition, supposed to record the paleoenvironment of the freezing process, was for the first time tried as a biomarker for paleoenvironmental reconstructions of ground ice formation. Parallel factor (PARAFAC) analysis of EEM (Excitation-Emission matrix) of fluorescent DOM decomposes four components: P1–P3, which are related to allochthonous humic-like constituents, and P4, which is relevant to autochthonous fraction associated with microbial activity. The distribution of fluorescent DOM tracked the variability in both paleoclimate conditions of the IW formation (discriminating the Holocene and the Late Pleistocene IWs) and types of ground ice (IW and TGI), which demonstrates the potential of the used approach.

Keywords: ground ice; ice wedges; paleoclimate; stable isotope; dissolved organic matter; methane; Faddeevsky; East Siberian Arctic

1. Introduction

✗The widespread ground ice in the Arctic often initiates cryogenic processes and contributes to permafrost disturbance [1]. Pre-aged labile organic matter (OM) release

upon permafrost degradation with coinciding and subsequent greenhouse gas emissions may affect current global warming due to methane-induced positive feedback [2]. The reservoir of organic matter in permafrost, isolated from the biogeochemical cycle, initially accumulated during primary production over a long period of time. Thus, by understanding the conditions of the permafrost formation, we can estimate the quantitative pool of organic carbon and its behavior upon thawing not only in a particular region, but also in areas with a similar Late Pleistocene and Holocene history. Previous studies [3–5] have displayed the higher potential of ground ice as a paleoenvironmental archive of the Late Pleistocene–Holocene. The most frequently used approach for identifying paleoclimate conditions is stable isotope analysis of ice wedges (IWs) due to the established relationship between $\delta^{18}O$ of precipitation and air temperature [5–9]. The ion composition of melted ground ice allows us to estimate the fluctuations in sea level due to the marine aerosol content, as well as to assess the contribution of terrigenous ions during ice wedge growth [4,10–12]. Research on the gas component, especially methane, has been used to define the origin of tabular (massive) ground ice (TGI) in Western Siberia [13,14]. Gas geochemical investigations in Eastern Siberia [15–17] have reported that concentrations of CH_4 and CO_2 in ice wedges reflect not only captured atmospheric air, but its production by biological activity. Molecular and fractional compositions of dissolved organic matter (DOM) are widely used for the study of carbon storage and cycling in the hydrosphere [18,19]. Considering that the composition of DOM, incorporated into the objects of the cryosphere, reflects the freezing environment [20–22], we use the fluorescent DOM (excitation–emission matrix, EEM) fractions deconvoluted by parallel factor (EEM-PARAFAC) analysis for ground ice characterization in terms of biogeochemistry and paleoclimate.

Despite the relatively extensive knowledge about the permafrost and ground ice of the New Siberian Islands [3,5,23,24], particularly in relation to Kotelny Island [3,25] and Bunge Land [26], there is a distinct lack of research on the ground ice of the Faddeevsky Peninsula. Most studies on the peninsula focused on identifying the origin of tabular ground ice, which is widespread in the Anju Islands [24,26–29]. According to A. Anisimov [30] and V. Tumskoy [24], the tabular ground ice on the Faddeevsky and New Siberia Island coasts represents a relic of a local ice sheet with the center on the De Long Islands [31] formed at the end of the Middle Pleistocene. Based on the geochemical composition of tabular ground ice of New Siberia Island, V. Ivanova [29] made an assumption about the injected origin of the lower horizon of ice, while the upper horizon was formed by segregation processes. Regarding IWs, the only comprehensive study of Yedoma Ice Complex (IC) deposits, including dating and stable isotope analysis of IWs and lens ice on Faddeevsky, was conducted in the section near the Khastyr River [32].
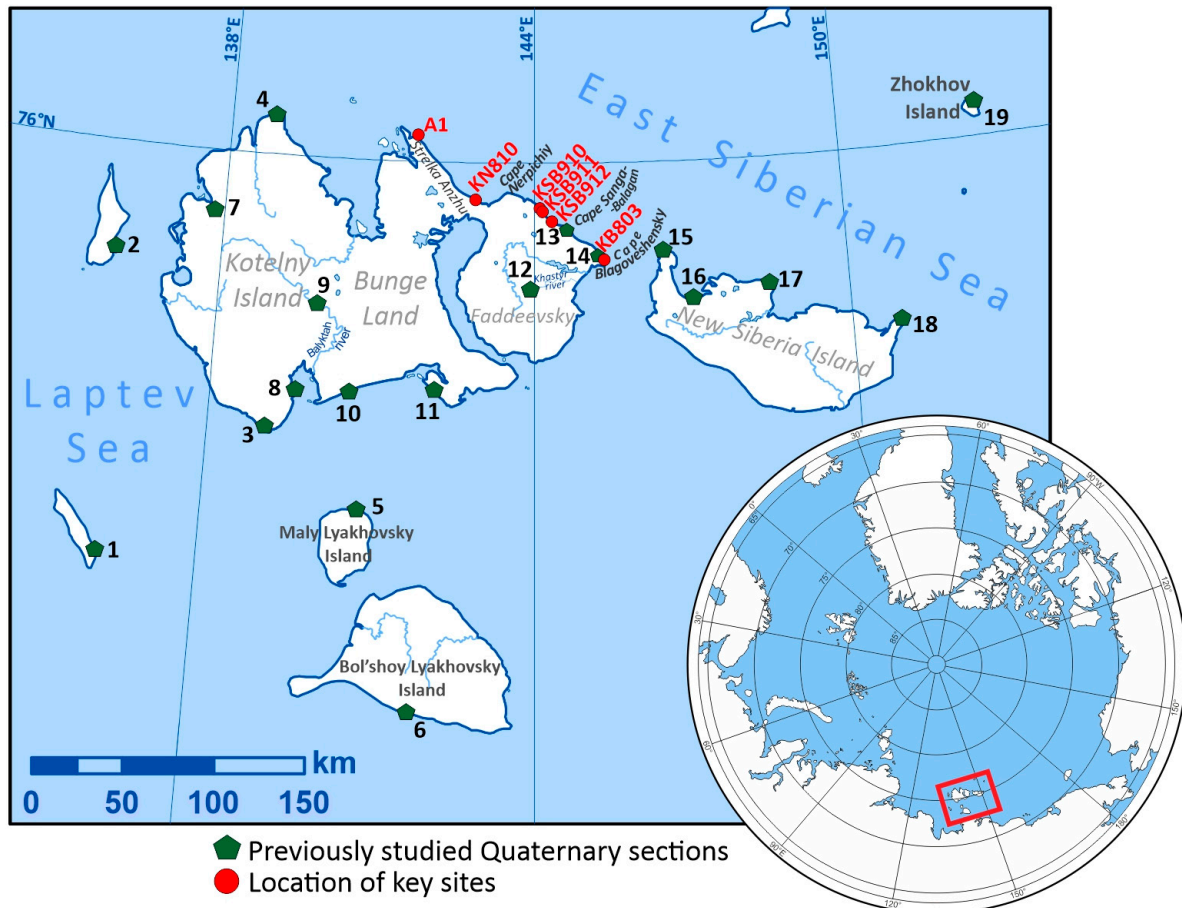
In order to address existing paleoenvironmental data gaps on the Faddeevsky Peninsula, we observed the isotope and ion composition, the content of methane and molecular composition of the gas component, bulk biogeochemical parameters (dissolved organic carbon (DOC), dissolved inorganic carbon (DIC), dissolved inorganic nitrogen (DIN), and the fractional composition of fluorescent DOM in ground ice samples. Our research aims to create paleoenvironmental reconstructions of the Late Pleistocene–Holocene for the Faddeevsky coast by implementing traditional and relatively new geochemical approaches to ground ice studies.

2. Study Area

Faddeevsky is the eastern peninsula of Kotelny Island, the largest of the New Siberian Islands archipelago. In many 19th and 20th century sources, before the exploration of Bunge Land, Faddeevsky was considered to be a separate island. Generally, the main part of the peninsula is a dissected, gently sloping accumulative denudation plain 20–30 m high, consisting of ice complex (IC) deposits. Faddeevsky entirely falls within the Arctic climate zone with an average annual air temperature of −15.4 °C and an average January temperature of −31.3 °C [32]. The peninsula is located within a continuous permafrost
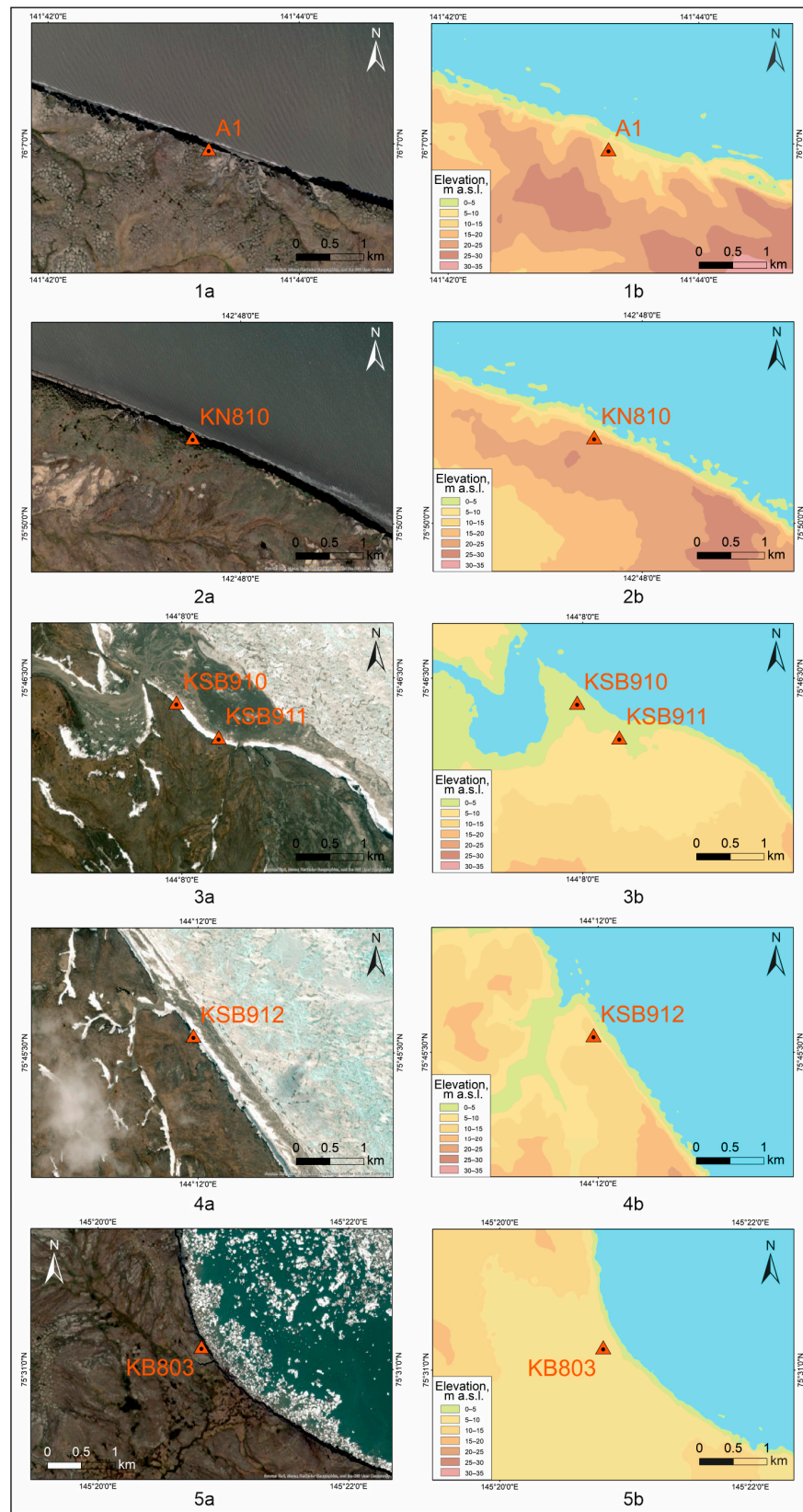
zone with mean annual ground temperatures between -14 and -9 °C. The predominant landscape is grass–moss polygonal tundra.

We studied different types of ground ice and enclosing Quaternary sediments on the low coast of the Faddeevsky Peninsula at four key sites (Figures 1 and 2): the Strelka Anzhu Peninsula (A1), the cape Nerpichiy (KN810), the cape Sanga-Balagan (KSB910; KSB911; KSB912), and the cape Blagoveshchensky (KB803).
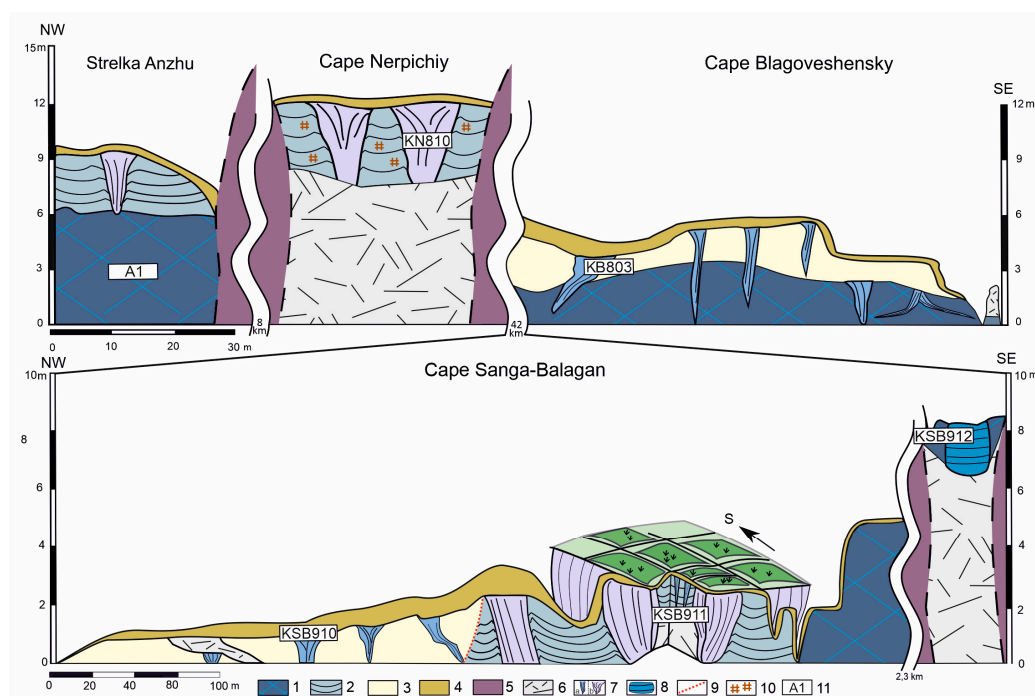

Figure 1. Study area and location of key sites. Previously studied Quaternary sections: 1—Stolbovoy Island; 2—Bel'kovsky Island; 3—Khomurganakh River, Kotelny Island; 4—Cape Anisii, Kotelny Island; 5—Maly Lyakhovsky Island [3]; 6—Bol'shoy Lyakhovsky Island [3,5,23,33]; 7, 8, 9—Kotelny Island [25,34]; 10, 11—Bunge Land [26]; 12—Khastyr River, Faddeevsky [32]; 13—Cape Sanga-Balagan, Faddeevsky [24,35–37]; 14— Cape Blagoveshensky [24,35,37]; 15, 16, 17, 18—New Siberia Island [24,29–31]; 19—Zhokhov Island [38].

We investigated the geochemical features of lens ice which formed reticulate cryostructure in a 10 m outcrop of the Strelka Anzhu Peninsula (Figure 1; A1). Enclosing marine clays and loams, known as deposits of the Kanarchak Formation, are traced along the coast at different heights [24,35]. The clays were epigenetically frozen, forming various types of cryogenic structure. The enclosing sediments are saline (the clay salinity is about 0.7%). Cl and Na predominate in the ion composition in accordance with their marine origin [37]. The age of the clays is controversial [24,29,35]. We assume that the clays studied at the key site A1 (Figure 3) formed during the transgression of MIS 5 [39] and froze after the sea regression in MIS 4, which is supported by the data provided by M. Alekseev [36] and V. Tumskoy [24].

Figure 2. Detailed location and relief of the Faddeevsky key sites (**1–5**) shown in Figure 1. Background images (**a**) are from world imagery ArcGIS base map provided by the Environmental Systems Research Institute—ESRI. Elevation maps (**b**) are from ArcticDEM mosaics data [40].

Figure 3. Schematic section of the studied key sites on the Faddevsky eastern coast. Legend: 1—marine deposits (clay and loam) with reticulate cryostructure; 2—Late Pleistocene Yedoma Ice Complex (IC) deposits; 3—Holocene deposits; 4—cover layer; 5—bedrocks (Paleogene–Neogene); 6—debris; 7—ice wedges (a—Holocene; b—Late Pleistocene); 8—tabular ground ice; 9—boundary between Holocene and Late Pleistocene deposits; 10—peat lenses and layers; 11—key sites.

Late Pleistocene Yedoma Ice Complex (IC) and Holocene deposits overlie the clays (Figure 2). To the east of the cape Nerpichiy (Figure 1), in the upper part of the 12 m cliff, two ice wedges are exposed at a distance of 5 m (Figure 3). The sampled IW (KN810) has a width close to 4–4.5 m and visible vertical extent of about 5 m. The enclosing sediments are represented by peat and organic-rich (TOC—4.7%) silty loams with layered cryostructure [37]. For the similar section in the Khastyr River area (Figure 1), dates in the range of 25.7–43 ka BP were obtained [32], indicating the formation of deposits during MIS 3. High-resolution imagery (Figure 2(2a)) shows baydzherakh (residual thermokarst mounds) relief typical on Yedoma upland slopes [41]. Therefore, we suggested studying the Late Pleistocene ice wedges of the Yedoma IC formation.

To the west of the cape Sanga-Balagan (Figure 1, KSB910, KSB911, KSB912), the Quaternary section consists of a sequence of ice wedges of different ages (Figure 3). At the lowest absolute levels (0.5–3 m a.s.l.), relatively small narrow ice wedges (up to 1.5 m in width and 2 m in vertical extent) are exposed, whereas the ends of some of them are below the beach level. In this part of the section, we sampled ice monoliths of the IW KSB910 in silty loams with layered cryostructure. To the east, with the rise of the coastal cliff height, Yedoma IC deposits (Figure 3) are exposed, later disappearing beneath the beach. It is difficult to estimate the size of the wedge, since the ice opens in a longitudinal section, forming a single ice "wall". The narrow (0.4 m width) epigenetic IW penetrates into the Late Pleistocene Yedoma IC to a depth of 2 m in the key site KSB911 (Figure 1). Then, 2.3 km south of KSB911 (Figure 1), between the outcrops of the Paleogene–Neogene bedrock, the tabular ground ice (TGI) is exposed in a 9 m coastal cliff (KSB912) (Figure 3). The TGI is transparent and coarse grained, with mineral inclusions unevenly distributed in the ice body. The enclosing silty clays are saline (the silty clays' salinity is 0.5%), and Na, Mg, and Cl ions dominate in the water solute composition [37].

The section near the cape Blagoveshchensky (Figure 1, KB803) has been significantly altered by thermal erosion and denudation processes (Figure 2(5a)). Along the entire coast,

different-aged IWs are exposed, while their size rises to the northwest with increasing coastal elevation. We study the lowest part of the coast at the key site KB803. Marine clays in the lower part of the section are overlapped by Holocene continental deposits with narrow syngenetic and epigenetic ice wedges. At the same time, the ends ("tails") of wedges are epigenetically included in the sequence of marine clays. In the eastern part of the section, there is an alluvial sequence of cross-bedded sands that cut off epigenetic ice wedges. We sampled the Holocene IW KB803 (Figure 3), the lower part of which was formed epigenetically in marine clays, whereas the upper part was grown syngenetically under continental conditions.

3. Methods

3.1. Fieldwork and Sample Preparation

During fieldwork conducted on the Faddeevsky coast, ice monoliths (30 samples) and frozen enclosing deposits were taken and transported to the analytical center of FSBI "VNIIOkeangeologia" (Saint Petersburg, Russia). To carry out the complex analytical studies, we applied an optimized scheme for subsampling and sample preparation [14]. Prior to analysis, separately from the gas component measurements, meltwater samples were transferred through a 0.45 μm syringe filter (Sartorius). All geochemical datasets analyzed for the ground ice samples of the Faddeevsky Peninsula are presented in the Supplementary Material (Table S1 in Supplementary material).

3.2. Stable Isotope Composition

Stable isotope data from ground ice meltwater samples were analyzed using the Picarro L2120-i analyzer at the Climate and Environmental Research Laboratory of the Arctic and Antarctic Research Institute (Saint Petersburg, Russia). Results were expressed in delta per mil notation (δ, ‰) relative to the Vienna Standard Mean Ocean Water (VSMOW) standard. The analytical precision is better than ± 0.3‰ for δD and ± 0.05‰ for $\delta^{18}O$.

3.3. Dissolved Gas Analysis, DOC, and DIC Measurements

Gas chromatographic (GC) analysis of C_1–C_5 hydrocarbon gases (HCGs) in the meltwater headspace was performed on a Shimadzu GC 2014 gas chromatograph equipped with 10-port gas valve with an evacuated loop, Restek Rt-Aluminia BOND/Na_2SO_4 (40 m) wide bore capillary column, and flame ionization detector (FID). Helium was used as carrier gas at a flow rate of 25 mL/min. To determine the concentrations of CO_2, we used a Porapak-N packed column (1 m) and a thermal conductivity detector (TCD).

The certified gas mixtures were used for instrument calibration. The uncertainty of the GC measurements was no higher than $\pm$ 5%. The detection limits were ~0.1 ppmV for methane and HC gases and ~1 ppm for CO_2. Methane concentrations (μmol) were calculated using the values of headspace mixing ratio and Bunsen solubility coefficients [42]. Gas wetness (gas wet percent, wetness coefficient, kW) was determined according to the formula ΣC_2–$C_5/\Sigma C_1$–$C_5 \times 100$ [43].

Dissolved carbon species (DOC and DIC) were measured using the Shimadzu TOC-V CSN element analyzer. The uncertainty of the analytical measurements was no higher than ± 6%. Detection limit did not exceed 0.05 mgC/L. To calculate the total DIC, we summarized the obtained values of DIC with a dissolved fraction of CO_2 in headspace.

3.4. Ion Composition, DIN Measurments

The ion composition of filtered meltwater samples was analyzed using ion chromatography with a Metrohm 940 Professional IC Vario with a conductometry detector and a chemical suppressor unit (MSM-A) to reduce the background conductivity. The anions were separated using a Metrosepp A Supp 5–250/4.0 column and 5 mmoL Na_2CO_3/$NaHCO_3$ solution as an eluent at flow rate 1 mL/min. The cations were separated with a Metrosepp C6–250/4.0 column and a mixture of 1.7 mM nitric and 1.7 mM dipicolinic acid solution as an eluent at a flow rate of 0.9 mL/min. The certified standard mixtures of ion com-

position (Fluka) were used to calibrate and calculate the resulting concentration values (mg/L). The uncertainty of the analytical measurements was ±1.5%. The detection limit was 0.02 mg/L (Cl^-).

To determine the non-sea-salt component of Ca^{2+} ([$nssCa^{2+}$]) and SO_4^{2-} ([$nssSO_4^{2-}$]), we used the following equations, assuming that Na predominantly originates from sea salt [11]:

$$[nssSO_4^{2-}] = [SO_4^{2-}] - a* [Na^+]; a = 0.198, \qquad (1)$$

$$[nssCa^{2+}] = [Ca^{2+}] - b* [Na^+]; b = 0.024, \qquad (2)$$

where a and b are the SO_4^{2-}/Na^+ and Ca^{2+}/Na^+ of regional sea water [29], respectively.

The total dissolved solute (TDS) content was determined as the sum of all ions and DIC. Dissolved inorganic nitrogen (DIN) was determined as a sum of NO_3^- and NH_4^+.

3.5. Fluorescence Measurements of Dissolved Organic Matter Molecular Composition

A Shimadzu RF5301 Fluorimeter was used for fluorescent excitation–emission matrix (EEM) measurements with wavelength ranges of 250–500 nm for excitation and 250–600 nm for emission. The excitation and emission wavelength steps were 2 and 1 nm, respectively. The inner filter effect was controlled by the sample dilution [44]. The diagnostic spectral indices, fluorescent index (FI), and biological index (BIX) were calculated [45].

The dissolved organic matter (DOM) fractional composition based on EEM spectra was explored by PARAFAC modeling using the Matlab graphical user interface (GUI) toolbox efc v1.2 (https://www.nomresearch.cn/efc/indexEN.html accessed on 19 July 2022). This toolbox was developed based on the n-way package in DOMFluor [46] and FDOMcorrection [47]. A dataset comprising 128 3D EEM spectra of the filtered ground ice meltwater samples was employed for PARAFAC modeling. The appropriate number of PARAFAC components was determined as result of the split-half validation procedure [48]. The relative concentration of each PARAFAC component in Raman units (RU) was estimated by the Fmax output of random initialization analysis [49]. The modified Tucker's congruence coefficient values (mTCC) were utilized to compare the identified PARAFAC components with library data containing 38 PARAFAC models [50]. The mTCC values of >0.95 reliably indicate a match between the two PARAFAC components.

4. Results

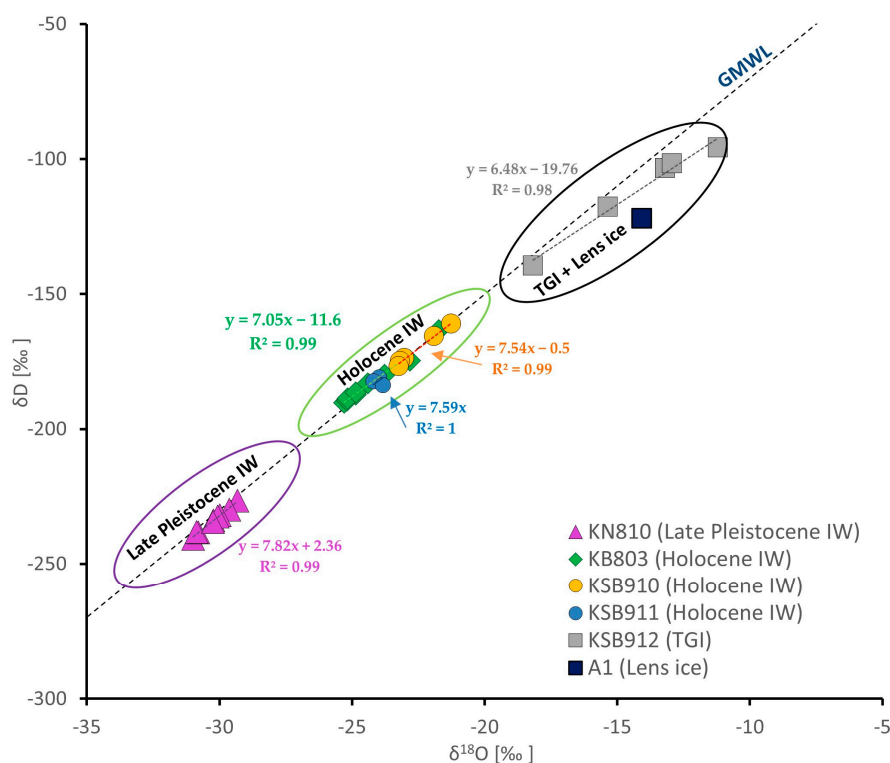### 4.1. Stable $\delta^{18}O$ and δD Isotopes

Table 1 provides an overview of stable isotope data for each type of ground ice.

Table 1. Stable isotope data of ground ice studied on the Faddeevsky coast.

Site	Type of Ice	$\delta^{18}O$ (‰)	δD (‰)	d-excess
KSB911	Holocene IW	−24.2 to −24.0; −23.8 *	−183.7 to −180.9; −182.3	7.0 to 11,3; 9.8
KB910	Holocene IW	−23.2 to −21.3; −22.5	−176.7 to −161.0; −170.3	9.1 to 10.7; 9.9
KB803	Holocene IW	−25.3 to −21.7; −24.2	−190.2 to −163.4; −182.6	7.9 to 12.7; 11.3
KN810	Late Pleistocene IW	−31.0 to −29.3; −30.2	−240.6 to −226.5; −234.0	7.2 to 8.8; 7.9
KSB912	TGI	−18.2 to −11.2; −14.2	−139.5 to −95.8; −111.6	−6.2 to 5.9; 1.8
A1	Lens ice	−14.1	−122.1	−9.5

* Min to max; average.

According to the position of the values on the $\delta^{18}O$–δD diagram (Figure 4), ice wedges, TGI, and lens ice formed three groups. The isotope values of different ice wedges (IWs) correlate well with the global meteoric water line (GMWL), which confirms their atmospheric origin and indicates equilibrium isotope fractionation during the formation of atmospheric moisture and wedge ice. Moreover, two groups of IWs can be identified: those with $\delta^{18}O$ values > −29‰ (KN810) and those with $\delta^{18}O$ values from −22.5 to −24‰ (KB803, KSB910, KSB911).

Figure 4. The δ^{18}O–δD diagram of the different ground ice from the Faddeevsky eastern coast.

In accordance with the previously published δ^{18}O data for this region [25,29,33,51,52], we have identified ice wedges formed in different periods of the Holocene (KSB911; KSB910; KB803) and Late Pleistocene (KN810). The Late Pleistocene IW is characterized by almost uniform distribution of values for δ^{18}O (−31 to −29.3‰), as well as a small range for δD (−240.6 to −226.5‰) and d-excess (7.2 to 8.8‰). Holocene wedges express a greater variability of stable isotope values. For KB803, the lowest value was recorded in the sample taken from the "tail" (KB803-9V, Table S1): −21.7‰ for δ^{18}O and −163.4‰ for δD, while for most samples, δ^{18}O was close to −25‰ and δD was approximately −129‰. KB803 has elevated d-excess up to 13 ‰. The KSB910 record indicates the same features, but with slightly high isotope values; the mean δ^{18}O was −22.5‰ and the mean δD was −170.3‰. The d-excess was close to 10‰. The most modern IW KSB911 had a mean of −24.0‰ for δ^{18}O‰ and −182.3‰ for δD. The d-excess values varied from 7 to 11‰ (Table 1).

The δ^{18}O–δD data of lens ice observed in the marine deposits of the Strelka Anzhu Peninsula (A1) and TGI of Cape Sanga-Balagan (KSB912) were below the GMWL, implying intrasedimental origin [4]. Compared to ice wedges, the TGI of KSB912 shows the highest values, ranging from −18.2 to −11.2‰ for δ^{18}O and −139.5 to −95.8‰ for δD (Table 1). The A1 sample shows similar data: −14.1‰ for δ^{18}O and −122.1‰ for δD (Table 1). The lowest d-excess including negative values were reported in the A1 sample (−9.5 ‰) and in the TGI sample KSB912-3 (−6.18‰, Table S1), while the mean d-excess value for KSB912 was about 1.8‰.

4.2. Carbon Cycle Parameters (DOC, DIC, CH₄, C₂–C₅ Gases)

Table 2 contains information about concentrations of dissolved carbon species (DIC and DOC), methane (CH₄), total content of hydrocarbon gases (HCG), and humidity coefficient (kW).

Table 2. CH$_4$ and CO$_2$ concentrations, parameters of C$_1$–C$_5$ HG molecular composition.

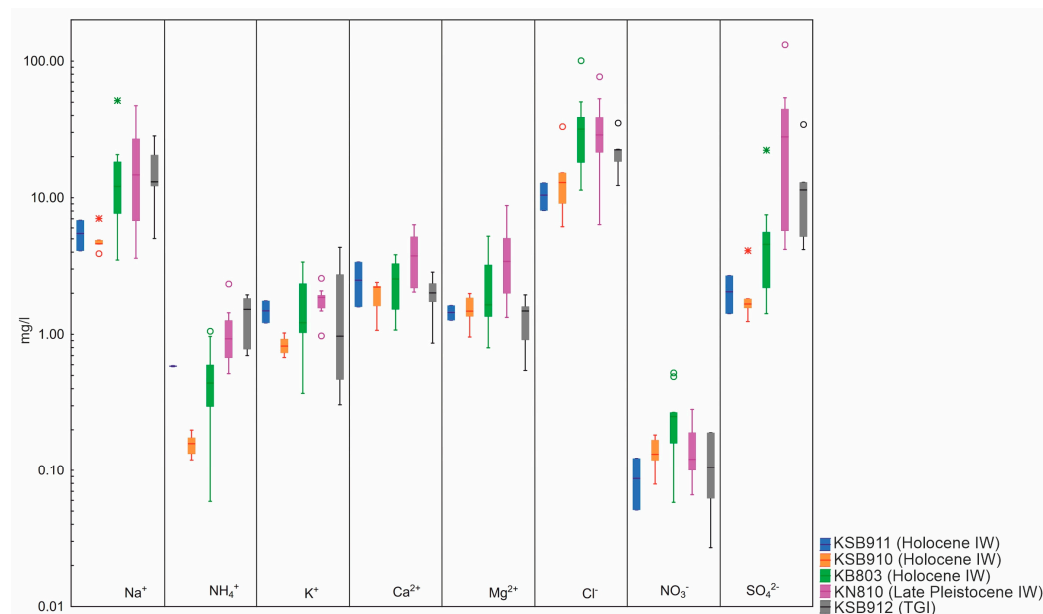| Site	Type of Ice	DOC, mg/L	DIC, mg/L	CH$_4$, μmol/L	Total HCG, ppm	kW, %
KSB911	Holocene IW	9.3 to 13.6; 11.4 *	2.1 to 4.9; 3.5	0.50 to 1.55; 1.06	12.6	0.7
KB910	Holocene IW	3.5 to 7.6; 5.0	2.0 to 5.7; 3.6	0.02 to 0.29; 0.11	1.5	6.7
KB803	Holocene IW	7.0 to 1.3; 8.6	1.0 to 3.2; 2.2	0.13 to 2.27; 0.80	11.4	1.1
KN810	Late Pleistocene IW	10.5 to 17.7; 13.5	3.4 to 6; 4.2	0.02 to 0.19; 0.07	1.2	25.7
KSB912	TGI	1.7 to 6.5; 4.2	0.9 to 1.3; 1.1	0.07 to 0.59; 0.23	3.4	1.7
A1	Lens ice	13.7	4.5	0.01 to 0.07; 0.05	0.7	5.4

* Min to max; average.

DOC concentrations in IWs ranged from 3.5 mg/L in the Holocene IW KB910 to 17.7 in the Late Pleistocene IW KN810. The highest DOC concentrations were found in the Late Pleistocene IW with a mean of 13.5 mg/L, in accordance with published data [53]. Holocene IWs showed a wide range of DOC values, with an average of 5 mg/L for KSB910, 8.6 mg/L for KB803, and 11.4 mg/L for the youngest epigenetic IW KSB911 (Table 2). Lens ice demonstrated DOC enrichment with 13.7 mg/L, while the DOC range for TGI was 1.7 to 6.5 mg/L (Table 2). DIC concentrations showed a smaller range of values from 0.9 mg/L in TGI to 4.5 mg/L in lens ice. Among the wedges, the highest values were found in the Late Pleistocene IW, with a maximum of 6 mg/L, although the Holocene ice showed slightly lower concentrations.

The methane concentrations in the samples varied from 0.01 μmol/L in the lens ice sample (A1) to 2.27 μmol/L in the IW sample KB803-2G (Table S1). KB803 was characterized by an uneven distribution of CH$_4$ with maxima in the range of 0.8–2.27 μmol/L in side samples taken along a horizontal profile in the upper part of KB803. The epigenetic IW (KSB911) demonstrated methane enrichment with a mean of 1.55 μmol/L compared to KSB910 and KB803. The Late Pleistocene IW was depleted of methane, revealing the maximum of 0.2 μmol/L (Table 2). CH$_4$ concentrations in most samples of intrasedimental ice did not exceed 0.1 μmol/L, excluding TGI samples KSB912-3 (0.59 μmol/L) and KSB912-4 (0.33 μmol/L) (Table S1).

4.3. Ion Composition and DIN

The ion composition of analyzed samples expressed the significant variability between different key sites, as well as within a particular ice body (Figure 5; Table S1).

Figure 5. Boxplot of major ion concentrations in ground ice samples.

TDS content ranged from 20 mg/L in the Holocene IW (KB803-6V, Table S1) to 344 mg/L in lens ice (A1); the average TDS concentrations of each site are detailed in Table 3. Generally, Holocene ice wedges are marked by lower TDS content with distinct peaks (local maxima), such as 190 mg/L in the "tail" sample of KB803-9V (Table S1). The Late Pleistocene IW (KN810) showed a wide range of TDS, with the highest values in the older (side) parts of the IW up to 252 mg/L (KN810-G4, Table S1). For this paleoenvironmental study, we used the ratios of major ions to TDS (Table 3), considering the wide range of TDS values. The Table 3 does not present PO_4^{3-}, NO_3^-, and Br^-, as their ratios do not exceed 0.6% for PO_4^{3-} and NO_3^- and 0.1% for Br^-. Some of the anomalies of these ions are discussed below.

Table 3. The average ratio of major ions to TDS (%), including non-sea-salt components of SO_4^{2-} and Ca^{2+}; TDS (mg/L) of key sites.

Site	Type of Ice	Na^+	NH_4^+	K^+	$ssCa^{2+}$	$nssCa^{2+}$	Mg^{2+}	Cl^-	$ssSO_4^{2-}$	$nssSO_4^{2-}$	TDS
KSB911	Holocene IW	19.8	2.1	5.4	0.5	8.5	5.2	37.9	3.9	3.5	27.6
KSB910	Holocene IW	16.3	0.5	2.7	0.4	5.8	5.0	49.9	3.2	3.5	30.7
KB803	Holocene IW	23.5	0.8	2.3	0.6	3.2	3.3	53.1	4.6	4.2	67.0
KN810	Late Pleistocene IW	17.7	1.1	1.8	0.4	3.2	3.9	31.6	3.5	32.1	101.1
KSB912	TGI	24.0	2.8	2.1	0.6	3.7	2.6	35.7	4.8	21.3	52.9
A1	Lens ice	41.0	0.8	2.6	1.0	0.7	1.7	42.5	8.1	0	344.2

The dominant part of the TDS in the studied samples is represented by Na^+ and Cl^- ions, ranging from 3.5 (the KB803-6V sample, Table S1) to 141.1 mg/L (the A1 sample, Table S1) for Na^+ and from 6.1 (the KSB910-5 sample, Table S1) to 146.4 mg/L for Cl^- (the A1 sample, Table S1). Samples from lens ice (the A1 sample, Table S1) and the "tail" of the KB803 IW (the KB803-9V sample, Table S1) demonstrate the highest concentrations of Cl^- (146.4 and 100.5 mg/L) and Na^+ (141.1 and 51.3 mg/L), respectively.

In the TDS composition of KN810, SO_4^{2-} prevailed, although the values were distributed unevenly across the ice body, ranging from 4.2 (the KN810-G2 sample, Table S1) to 131.6 mg/L (the KN810-G4 sample, Table S1). Meanwhile, the SO_4^{2-} concentrations in KSB912 ranged from 4.2 (the KSB912-5 sample, Table S1) to 34.3 mg/L (the KSB912-2 sample, Table S1). Remarkably, the Late Pleistocene IW (KN810) and TGI showed $nssSO_4^{2-}$ enrichment, while SO_4^{2-} records from other sites reflected the "marine" signal. Among Holocene wedges, SO_4^{2-} did not exceed 7.49 mg/L, except for the KB803 "tail" sample, where the value reached 22.3 mg/L (KB803-9V, Table S1). The SO_4^{2-} in lens ice fully reflected the "marine" composition with a concentration of 28 mg/L (Table S1).
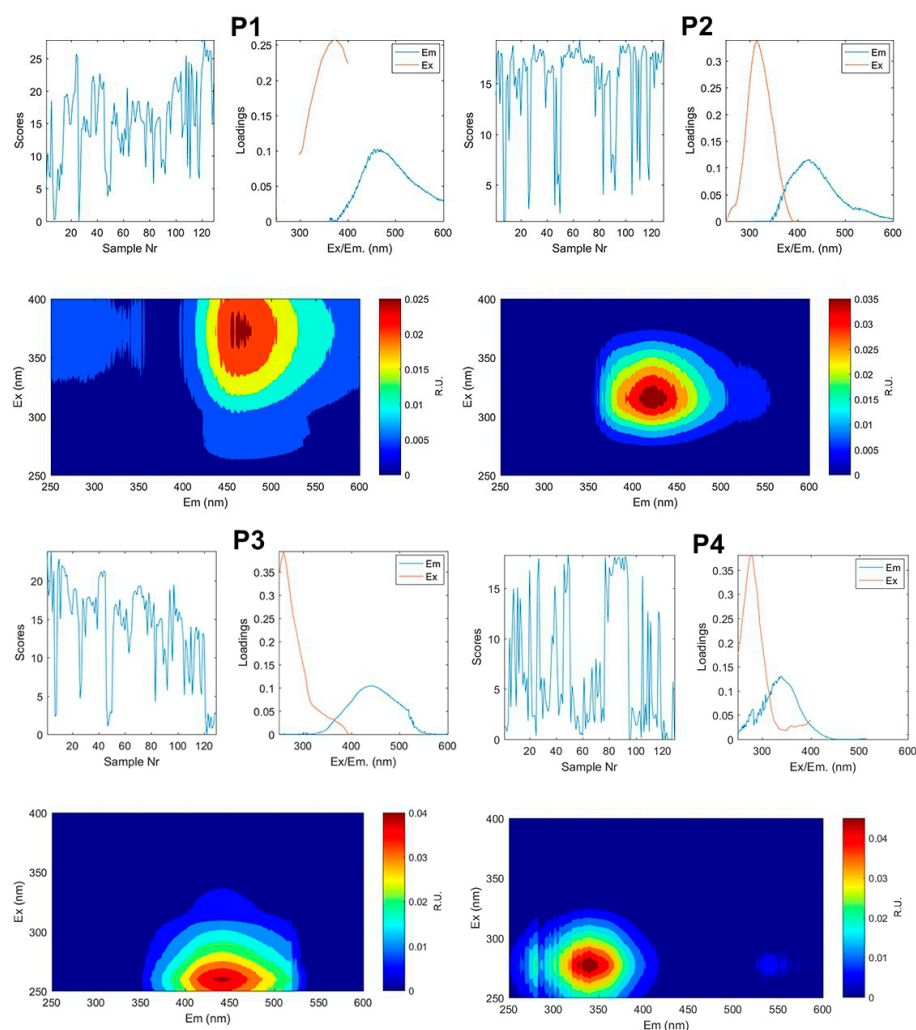
Ca^{2+} is mainly represented in non-sea-salt components, except lens ice (A1). Total Ca^{2+} was evenly distributed between the samples from 1.1 (the 803-6V sample, Table S1) to 6.3 mg/L (the KN810-G4 sample, Table S1). A close range was recorded for K^+ and Mg^{2+} ions, reaching 3.4 mg/L (in the sample KB803-9V, Table S1) and 8.75 mg/L (in the sample KN810-G5, Table S1), respectively. The lens ice (A1) shows a K^+ peak (9.1 mg/L) and a high Mg^{2+} content (6 mg/L).

Regarding Br^- concentrations, in most samples, they do not reach 0.1%; however, it should be noted that samples from lens ice and from the "tail" of KB803 show distinctive values: 0.4 and 0.2 mg/L (KB803-9V, Table S1). PO_4^{3-} enrichment was recorded in the KB803-4G sample (2.7 mg/L) and one KN810-G1 sample (1.6 mg/L), while the rest averaged 0.1 mg/L. The highest concentration of NH_4^+ was detected in lens ice A1 (2.8 mg/L), TGI (average value 1.5 mg/L), the "tail" sample KB803-9V (1.1 mg/L), and in KN810 (from 0.5 mg/L up to 2.3 mg/L) (Table S1), while a significant ratio of NH_4^+ to TDS dominated in ice formed epigenetically (KSB911 and KSB912) (Table 2). NO_3^- was found in all ground ice samples, with a maximum concentration of 0.5 mg/L in the Holocene IW KB803 (KB803-5G, Table S1).

The concentration of dissolved inorganic nitrogen (DIN) ranges from 0.1 mg/L in the IW KB803 (KB803-6V, Table S1) to 2.9 mg/L in lens ice sample (A1). Generally, Holocene IWs are characterized by low mean values of DIN: 0.8 mg/L in KB803; 0.3 mg/L in KSB910; and 0.7 mg/L in KSB911. The Late Pleistocene IW KN810 shows a wide range of DIN values from 0.7 to 2.4 mg/L. Relatively high DIN concentrations were found in TGI and lens ice, with mean values of 1.6 mg/L in KSB912 and 2.9 mg/L in A1 (Table S1).

4.4. Fluorescent DOM (fDOM) Composition and Fluorescent Indices

Four fluorescent components of DOM were extracted as result of the PARAFAC analysis. The component P1 (Figure 6) had an excitation wavelength ranging from 300 to 420 nm (maximum at 370 nm) and an emission wavelength ranging from 380 to 600 nm (maximum 470 nm). The library comparison analysis (efc v 1.2) indicated the exact correspondence of this component ($p = 0.989$) to the library fluorophore, which was described as a high-molecular-weight high-aromaticity humic DOM fraction of terrestrial origin [54]. The loadings (Fmax) varied from 0.26 RU in the IW sample KN810-V4 (Table S1) to 0.55 RU in the ice wedge sample KSB910-1 (Table S1). The median value of this component constituted 0.37 RU, which corresponded to 19.17% of the average bulk content of the fluorescent DOM defined as a sum of the PARAFAC components loadings. The coefficient of variation was equal to 14.62%.
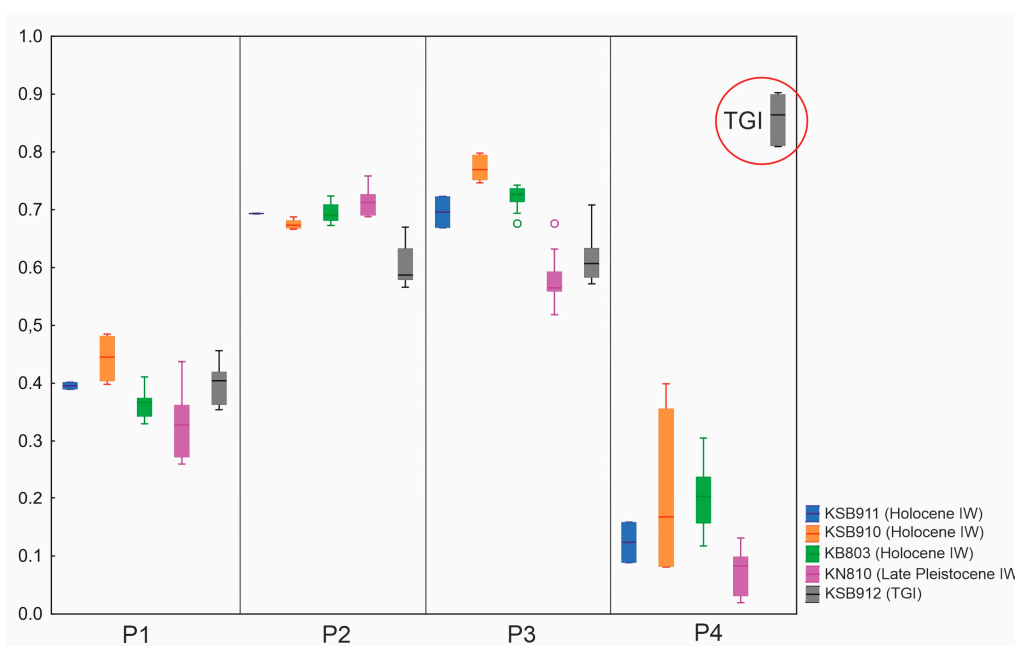

Figure 6. PARAFAC components and their characteristics. The top left graph represents the scores of the corresponding identified component; the top right graph indicates the excitation (Ex) and emission (Em) 2D spectra of each PARAFAC component.

The component P2 (Figure 6) had an excitation wavelength ranging from 270 to 380 nm (maximum at 310 nm) and an emission wavelength ranging from 370 to 500 nm (maximum 425 nm). The library comparison analysis (efc v 1.2) indicated the correspondence of this component ($p = 0.963$) to the library fluorophore, which was described as a humic-like DOM fraction associated with recent biological activity [55]. The loadings (Fmax) varied from 0.57 RU in the TGI sample KSB912-1 (Table S1) to 0.76 RU in the IW sample KN810-G5 (Table S1). The median value of the P2 component was 0.69 RU, which corresponded to 33.98% of the average bulk content of fluorescent DOM defined as a sum of the PARAFAC component loadings. The coefficient of variation was equal to 6.87%.

The component P3 (Figure 6) had an excitation wavelength ranging from 250 to 350 nm (maximum at 260 nm) and an emission wavelength ranging from 350 to 520 nm (maximum at 470 nm). The library comparison analysis (efc v 1.2) indicated the exact correspondence of this component ($p = 0.993$) to the library fluorophore, which was described as a ubiquitous humic-like DOM fraction of terrestrial origin [54]. The loadings (Fmax) varied from 0.52 RU in the IW sample KN810-V4 (Table S1) to 0.80 RU in the IW sample KSB910-2 (Table S1). The median value of the P3 component constituted 0.67 RU, which corresponded to 33.71% of the average bulk content of the fluorescent DOM defined as a sum of the PARAFAC component loadings. The coefficient of variation equaled 12.35%.

The component P4 (Figure 6) had an excitation wavelength ranging from 250 to 320 nm (maximum at 270 nm) and an emission wavelength ranging from 250 to 400 nm (maximum at 340 nm). The library comparison analysis (EFC v 1.2) indicated the exact correspondence of this component ($p = 0.987$) to the library fluorophore described as protein-like DOM [56]. The loadings (Fmax) varied greatly, ranging from 0.06 RU in the IW sample KN810-V2 (Table S1) to 0.90 RU in the TGI sample KSB912-5 (Table S1), comprising a maximum loading value of all quantified PARAFAC components in the sample collection. It presented Ks values of 0.95 and 0.94, with fluorescent peaks B and T indicating tyrosine-like and tryptophan-like fluorophores, respectively [57], calculated by fraction regional integration [49]. The median value of the P4 component was moderate (0.16 RU) relative to the humic-like DOM constituents above, which corresponded to 19.84% of the average bulk content of the fluorescent DOM defined as a sum of the PARAFAC component loadings. The coefficient of variation was extremely high, constituting 101.18%, which is linked to five-fold enrichment in the P1 component of the TGI (KSB912) relative to all sampled IWs.

Next, the extracted PARAFAC components P1–P3 were related to soluble humic-like substances, while P4 represented the protein-like DOM linked to free aromatic amino acids or polypeptide chains of the dissolved proteins. The greatest variation in fluorescent DOM composition was associated with pronounced enrichment of the tabular ground ice samples with a protein-like DOM fraction. The box plot in Figure 7 illustrates the bulk composition of the fluorescent DOM based on the EEM-PARAFAC analysis. We explored the variation in the PARAFAC components P1–P4 in the analyzed ground ice samples using the Kruskal–Wallis multiple ANOVA test. The results of the statistical test indicated significant variance ($p = 0.0066$) in concentrations (loadings) of the P1 component between the ice wedges KN810 and KSB910. The component P2 concentration was significantly lower ($p = 0.0001$) in TGI samples (KSB912) than in all the other sampled IWs. Among IWs, we observed that KN810 was sufficiently enriched in P2 compared to KSB910. The P3 component was of a significantly higher level ($p < 0.0001$) in the IW KSB910 than in all the other ground ice samples, including TGI. Meanwhile, the IW KN810 and the TGI KSB912 were considerably more depleted in the P3 component than the IWs KSB910, KSB911, and KN803. The P4 component was remarkable for more than five-fold enrichment in the TGI compared to IWs. We also observed relative depletion of the IW KN810 in protein-like DOM, which was considered insignificant according to Kruskal–Wallis ANOVA.

Figure 7. The box plot of the bulk composition of the fluorescent DOM based on the data of EEM-PARAFAC analysis.

The values of the fluorescent index (FI) varied from 1.14 (IW sample KB803-6V, Table S1) to 1.55 (IW sample KN810-G4, Table S1) with a coefficient of variation of 5.61%. We found no significant variance in FI between the sampled IW and TGI. The values of the normalized humification index (HIXc) ranged from 0.29 in the TGI sample KSB912-5 (Table S1) to 0.94 in the IW sample KN810-V2 (Table S1) with a coefficient of variation value of 21.24%. The results of the Kruskal–Wallis test show significantly higher humification of the IW KN810 relative to TGI (KSB912) ($p < 0.001$). The biological index (BIX) values varied between 0.47 in the IW sample KB803-5G and 1.45 in the TGI (KSB912) sample, with a coefficient of variation as high as 22.97%. The values of BIX were significantly higher in the TGI samples than in all of the IWs except for KSB911.

5. Discussion

5.1. Paleoclimate Record from Ice Wedges of the Faddeevsky Coast Based on $\delta^{18}O–\delta D$ Composition

According to previously published radiocarbon dates [3,25,32], ice wedges on Kotelny Island were formed during the Late Pleistocene (MIS 3 and MIS 2) and the Holocene (MIS 1). Generally, Late Pleistocene IWs of Kotelny and Faddeevsky recorded a wide range of $\delta^{18}O$ values from −31‰ to −25‰ [25,32], reflecting the large variability in winter air temperatures during that time. The insignificant difference in stable isotope data between IWs formed in MIS 3 and MIS 2 is related to the lack of a last glacial maximum (LGM) record [58]. The most recent data from the Bol'shoy Lyakhovsky IWs [33] represent the most depleted $\delta^{18}O$ (−37‰) in ice wedge records formed during the LGM. The mean $\delta^{18}O$ reported for Holocene IWs on Kotelny is about –23‰, while the variations in $\delta^{18}O$ do not exceed 2‰ [25].

Our $\delta^{18}O$ data from IWs of the Faddeevsky eastern coast broadly comply with the previously published information; however, some distinct features were revealed. $\delta^{18}O$ values of the KN810 IW were close to −30‰ and did not demonstrate significant variations compared to the Holocene wedges, where the changes in values of $\delta^{18}O$, even within a particular IW, reached 4‰. The observed variations in oxygen isotope signatures could be linked to temperature fluctuation during ice wedge growth or mixing of waters entering the wedge. For instance, heavier isotopic values (−22‰) in the "tail" of KB803 may be associated with possible ingress of sea water and sea level close to modern values in the early stages of IW growth. The Holocene ice wedges of Faddeevsky have a heavier

isotope composition by an average of 6‰ in comparison with those of the Late Pleistocene age; however, the average values obtained are slightly higher than those recorded on Kotelny Island [25], which can be explained by more severe climate conditions of the East Siberian coast.

The Holocene IWs are distinguished from the Late Pleistocene ones not only by heavier $\delta^{18}O$ values, but also by the highest mean d-excess of 11–13‰. Generally, d-excess alterations have been interpreted as a change in moisture sources or certain local processes as fractionation in the snow cover. Previous studies have interpreted these variations as an overrepresentation of early winter snow in the meltwater-fed IWs [58], the increased impact of the Atlantic, as well as the long-range transport of air masses on the Holocene snow cover [25].
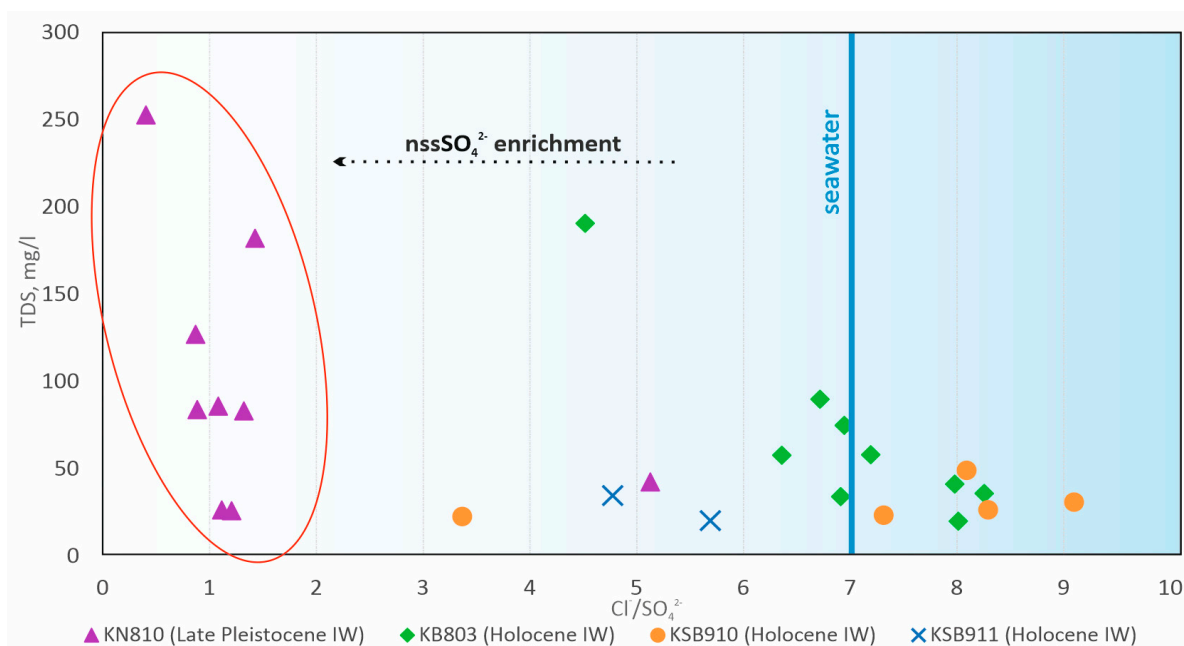
Temperature estimates [6] for the studied coast revealed that the mean temperature for MIS 3 dropped to -45 ± 3 °C in January, while in the Holocene, it was around -35 ± 3 °C. The higher winter temperatures of the Holocene reflect the influence of the sea and the warmer Atlantic masses. During the Holocene IW formation, temperature fluctuations were more pronounced than during MIS 3; mean January temperature varied from -38 to -31 °C. Thus, in the warmest periods of the Holocene, the January temperature was comparable to the modern value of -31 °C [32].

5.2. Ion Composition of Ground Ice for Paleoenvironmental Reconstructions

The ion concentrations of ground ice largely reflect the conditions of the formation period and freezing features. The most common approach used to establish paleoenvironmental conditions using ion analysis is to determine the "marine signal" in total dissolved solute (TDS) composition. Sea-salt ions are transported as part of marine aerosols generated by sea spray from open water, upward migration from sea ice, and frost flowers being wind-blown to the snow surface [59]. Na^+, Cl^-, and Br^- ions primarily originate from sea salt. Their common source is confirmed by a strong positive correlation ($Ks \sim 0.9$). Geochemical results from Western Siberia [4] identified the coastline position of the Kara Sea in the Late Pleistocene and Holocene based on estimation of the Cl^- and Na^+ enrichment. In order to assess the contribution of marine ions to the source water of studied IWs, we used the Cl^-/SO_4^{2-} plot (Figure 8) and clearly distinguished two groups of IW samples relative to seawater ratio [29], marked on the plot as a vertical blue line. The first group represented the Holocene ice wedges KB803 and KSB910, in which the Cl^-/SO_4^{2-} values were close to those of sea water. The predominance of Cl^-, Na^+, and $ssSO_4^{2-}$ in TDSs is indicative of the major contribution of sea-salt aerosols, suggesting the formation of the ground ice under strong marine influence in proximity to the coast. The direct participation of sea water in ice wedges is controversial; however, Yu. Vasil'chuk et al. [60] reported that TDS content of more than 200 mg/L may be a sign of sea or lagoon water. From this perspective, the "tail" sample of the KB803 IW featuring TDSs of more than 190 mg/L and anomalously high concentrations of marine ions may indicate ingress of sea water during early IW growth.

The second group (Figure 8), marked on the plot as a red oval, unites almost all samples of the Late Pleistocene IW, demonstrating the greatest $nssSO_4^{2-}$ enrichment. Such a high concentration of $nssSO_4^{2-}$ (86% on average) may be associated with mineral leaching of deposits (for instance, gypsum), background volcanism [61], or the oxidation of dimethyl sulfide (DMS) from marine phytoplankton in sea water [62]. Another likely source of $nssSO_4^{2-}$ is oxidation of the pyrite (FeS_2) which previously accumulated within marine deposits due to sulfate reduction. The subsequent weathering of the denudated sediments may lead to sulfate enrichment in the ground ice source water [63]. The relatively low ratio of marine components to TDS is likely indicative of the KN810 IW formation under continental conditions coupled with sea regression, similar to the ice wedges of Bol'shoy Lyakhovsky Island [10]. However, the impact of the sea on the studied coast is much more visible than that in other ice wedges of North Yakutia and the New Siberian Islands, as it is located closest to the Arctic Ocean. The IW KSB911 and individual samples from KSB910, KB803, and KN810, comprising a transition between the allocated groups, indicate that the

early stages of IW formation involved higher rates of $nssSO_4^{2-}$ than the samples of the first group [64]. The contribution of mineral particles is also determined by the Ca^{2+}/Mg^{2+} ratio in ground ice samples, which is higher than in sea water. $nssCa^{2+}$ enrichment in KSB911 is associated with epigenetic freezing through close contact with the host sediments and active layer. Generally, the accumulation of non-sea-salt components may also be related to the contact of spring snowmelts with the surface and the active layer, as well as the lateral contact of wedge ice with sediments, containing clay minerals, gypsum (Ca^{2+}), dolomite ($CaMg_2$), and feldspar (K^+) [11,65].

Figure 8. Cl^-/SO_4^{2-} ratio to Total Dissolved Solute (TDS) content in studied ice wedges.

The strongly saline lens ice of the 8 m high terrace in the area of the Anzhu Peninsula most likely reflects the composition of flooded marine deposits of the Kazantsevo transgression [36]. The TGI studied in the Sanga-Balagan area is fresh; the elevated TDS values are associated with $nssSO_4^{2-}$. Furthermore, the ion composition of the TGI from KSB912 coincides with the composition of the lower horizon of the TGI of New Siberia Island [29].

NH_4^+ in studied ground ice samples may appear from the snowpack, surrounding bedrock ("geological nitrogen") and organic matter decomposition coupled with ammonification [66]. Relatively high NH_4^+ concentrations in Late Pleistocene IWs might be associated with bedrock leaching, similar to $nssSO_4^{2-}$. Meanwhile, the high NH_4^+ content in the TGI samples is likely linked to active ammonification processes due to the lack of limitation of the autochthonous microbiota in the available nitrogen. This is consistent with the data on strong enrichment of TGI samples with autochthonous organic matter, according to the EEM DOM data. NO_3 in ground ice is probably derived from wet and dry atmospheric deposition, ammonification, and nitrification of soil organic matter and the oxidation of geologic ammonium [66].

5.3. DOC, DIC, and Methane Features in Different Types of Ground Ice

Generally, higher DOC concentrations in ground ice indicate more favorable vegetation conditions during its formation and a greater degree of soil–water contact. The Late Pleistocene IW appear to be relatively enriched in DOC. According to palynological data from Kotelny, within this period, local forest groups grew along the river valleys, while steppe or tundra-steppe landscapes were preserved on the watersheds, indicating better conditions for primary production [34,67]. Moreover, from 28 to 18.9 ka BP, New Siberia Island had better conditions for continuous peat formation [28]. Generally, winters in the

cold periods of MIS 3 in the study region were even colder than winters in MIS 2 (except during the LGM period), while the conditions of the growing season during the Karginsky interval (MIS 3) were significantly more favorable [34]. Enclosing deposits and active layers contribute significantly to the input of DOC into ground ice. Thawing processes in the active layer during seasonal or global climate variations suggest that high microbiological activity is responsible for both DOC mineralization and autochthonous production [68]. The Holocene IWs reveal lower DOC concentrations, with local exceedances in selected samples. Temperature increases on Kotelny Island in the Holocene contributed to the spread of shrub vegetation, while the lower summer temperatures led to the spread of wormwood–cereal plant associations [25]. Lower DOC concentrations in ice wedges and TGI can be explained by limited carbon inputs [69] or higher loss of organic matter through mineralization. Higher DOC concentrations in lens ice than in tabular ground ice are associated with prolonged contact of soil moisture with organic matter prior to freezing [53].

Spring snowmelt water, as the main source of wedge ice, comes into contact with vegetation and soil, leaching the soil DOC [51,70]. We found a moderate positive correlation (Ks > 5) between DOC and terrestrial ions (K^+, Mg^{2+}, $nssCa^{2+}$, and $nssSO_4^{2-}$), suggesting a common origin for these components [51]. The strong positive correlation between $nssSO_4^{2-}$ and DOC (Ks = 0.8) in the Late Pleistocene IW may indicate the single transport stream, leaching DOC and terrestrial ions.

DIC enrichment in ground ice may be associated with organic carbon mineralization, mainly due to aerobic respiration by local biota, or with dissolution of carbonate minerals as a result of the soil leaching carried out by the source water. Regardless of the relative contribution of each of these processes, we examine DOC/DIC as an important tracer of the carbon cycle. A comparison of the DOC/DIC ratios from the Yamal Peninsula [14] and the samples from Faddeevsky (present study) showed that the values of Yamal ground ice are reliably lower than those of Faddeevsky, as shown by the Kruskal–Wallis test ($p = 0.0018$). One of the possible explanations for this is the comparatively warmer climatic conditions and higher activity of respiring microbiota (Figure 9) in the lower-latitude Arctic region, which determines the higher rate of OM mineralization in ground ice from the Yamal Peninsula compared to Kotelny Island.
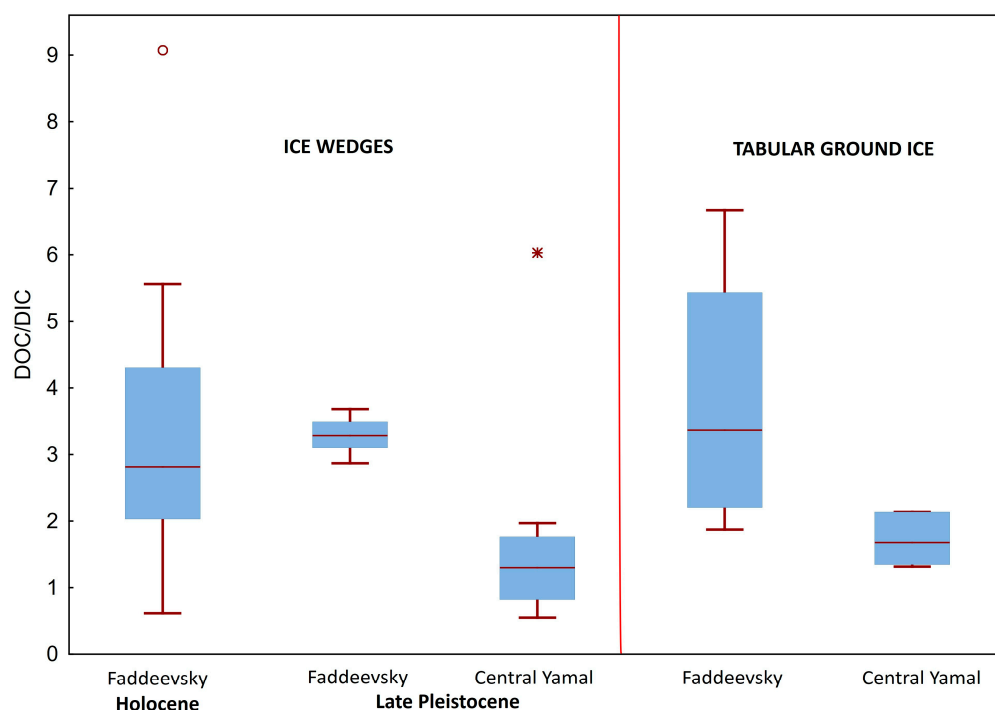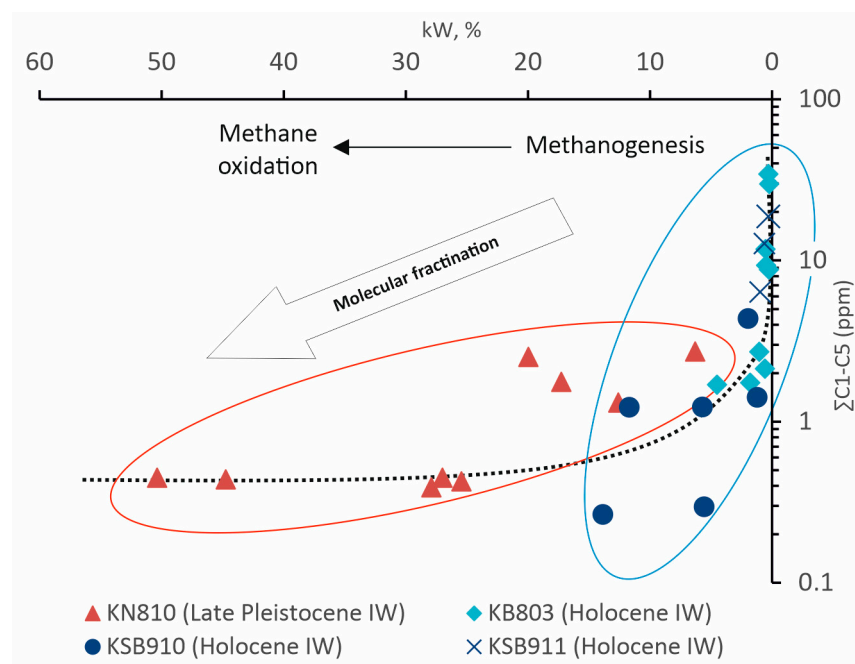

Figure 9. DOC/DIC ratio in ground ice from the Faddeevsky coast and the Yamal Peninsula [14].

The contrast between the Late Pleistocene and Holocene is illustrated by the lower methane concentrations in Late Pleistocene IW than in Holocene IWs, which was also reported for Western Siberia IW [13]. However, the CH_4 concentrations of IWs from the cape Mamontov Klyk reveal the opposite pattern [16]. The CH_4 mixing ratios are much higher than the atmospheric value, suggesting microbial methane production prior to their occlusion in IWs or under cryogenic conditions within the ice body, which is confirmed by low concentrations of heavy HCGs. It is well known that heavier homologues (mainly C_2–C_3) accompany microbially generated methane, though in incomparably low concentrations [71]. Thus, a depletion of the produced methane due to the subsequent microbial oxidation (aerobic or anaerobic) could be reflected in a relative increase in the C_2–C_3 components indicated by the elevated values of the gas wetness coefficient (kW, %) [71]. The elevated kW values in the samples of the Late Pleistocene IW KN810 (Figure 10) may be associated with preferential methane oxidation in the source water environment, or later during melting–refreezing and under cryogenic conditions. Microbial community cycling methane is abundant in the Yedoma deposits of Northeastern Siberia, as shown via the metagenomic study conducted in [72]. The various trends of the sample distribution across the headspace diagram likely distinguish Late Pleistocene and Holocene ice wedges in terms of the peculiarities of the methane cycle.

Figure 10. Headspace diagram of C_1–C_5 HG in IW samples (modified after [43]).

In Western Siberia, CH_4 concentrations serve as indicators of intrasedimental TGI formation [13]. Our data on the CH_4 content in TGI cannot indicate the origin of ice. However, CH_4 concentrations in the TGI found near the cape Sanga-Balagan were significantly lower than in the Yamal Peninsula.

5.4. DOM Fluorescence Properties of Ground Ice

We interpret the variations in the ground ice fluorescent DOM composition as signatures of changes in paleoclimate conditions. It can be assumed that each PARAFAC component (P1, P2, P3, P4) represents a specific pool of DOM assigned either to its biogenic producer or to a secondary process caused by initial DOM transformation before being incorporated into the ground ice. All the deconvoluted fluorophores exhibited spectral characteristics similar to those described in previous studies, suggesting the existence of common sources of DOM across latitudes. The EEM-PARAFAC data had high potential to differentiate between the characteristic features of the ground ice; this was supported

by the statistically significant variations between the studied IW and TGI in terms of the modeled components P1–P4.

In our study, the P4 component was significantly correlated (Ks > 0.9) with both amino acid fluorophores: tryptophan-like (peak T) and tyrosine-like (peak B) DOM detected by fraction regional integration (FRI). The corresponding protein-like DOM fraction was definitely linked to a local biota which produced, transformed, and excreted the OM [55]. The correlation between protein-like DOM and the percentage of biodegradable organic carbon (BDOC) in the DOM pool was previously demonstrated in a range of Alaskan freshwaters, indicating that the corresponding DOC fraction was the most biochemically labile and easily converted into CO_2 [18,19]. The five-fold enrichment of TGI in the P4 component compared to the IW detected in the present work might be a feature of epigenetic freezing, conserving the environment with abundant microbial life with unrestricted nutrient availability. TGI samples also demonstrate relatively high content of NH_4^+, which is allegedly a product of ammonification. Despite the lower content of DOC in the sampled TGI compared to IWs, the former is likely characterized by higher-quality organic matter.
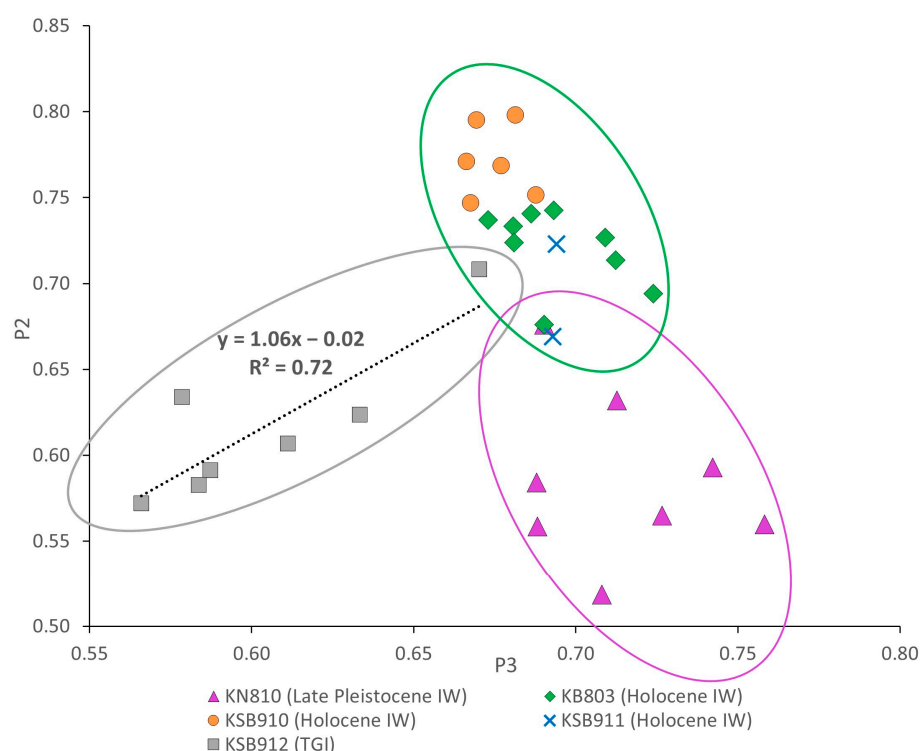
The humic components are predominantly, but not solely, assigned to allochthonous DOM derived from terrestrial plants biomass [19]. The most likely way to incorporate humic DOM into the forming IW is through leaching of the soil material from the overlying active layer and/or enclosing deposits. Thus, apart from a vegetation intensity responsible for net OM production, the factors favoring the export of terrestrial DOC into ground ice deposits are the hydrological transport and melting–refreezing processes.

The humic component P2 was remarkable due to its positive correlation with the DOC (Ks = 0.76). Moreover, we observed a moderately significant correlation of this component (Ks > 0.6) with the cations Mg^{2+}, Ca^{2+}, and K^+. This can be indicative of a preferentially terrestrial origin of DOC in the studied ground ice.

Comparing our results to the available data on EEM-PARAFAC components in the cryosphere, we conclude that the distribution of the DOM fractions in ice wedges from Faddeevsky was generally similar to those detected in ice wedges in East Siberia [21]. There was a strong prevalance of humic-like DOM over protein-like forms in terms of both quantity and diversity. Three humic-like and one protein-like EEM-PARAFAC component were detected, while Vonk et al. [21] discovered one protein-like and six humic-like components. The P2, P3, and P4 components of our study are generally consistent with KW4, KW2, and KW7 components, detected in the IW of lower Kolyma Yedoma [21]. The glacial-derived fluorescent DOM, as opposed to those of the ground ice, is preferentially enriched in the biolabile component, but extremely depleted in DOC content. The mean concentrations of DOC in the ground ice meltwater appear to be ~20 times lower in the glacier meltwater, as follows from the present study and numerous previous works [20,21]. However, among the humic-like DOM, the EEM-PARAFAC components P2 and P3 in our work likely coincide with the component C425 [20] and component 3 [22], respectively, both of which were found in the glacial meltwater samples. All the protein-like EEM-PARAFAC components predominant in glacial systems are largely similar to a blue-shifted component P4 of our ground ice samples. The above features suggest the integrity of the global sources of DOM in the cryosphere.

In order to discriminate the paleoclimate environments of the studied ground ice formation based on the fDOM data, we created scatter plots of the selected humic components P2 and P3 (Figure 11). As shown by the plot, there were three more or less distinct groups of samples, which are marked by ovals. The largest group included the Holocene IWs: KB803, KSB910, KSB911, characterized by the similar values of P2 and P3 with fairly compact distribution. The second group included only the samples of the TGI KSB912, representing relatively lower loadings of both P2 and P3 greatly scattered across the plot and positively correlated with each other (R^2 = 0,72). This correlation points to a common route of these components prior to freezing, and their conservation likely indicates epigenetic freezing during TGI formation. The third group formed by the lower loadings of P2 and higher values of P3 was represented by the Late Pleistocene IW (KN810). The resulting

distribution pattern clearly illustrated that the DOM signatures tracked the variability in both paleoclimate conditions of the IW formation (discriminating the Holocene and Late Pleistocene IWs) and types of ground ice (IW and TGI), likely linked to a different freezing mechanism (syngenetic and epigenetic). The two groups of IWs do not demonstrate a significant correlation between the components; however, we suggest (especially for the Holocene IW group) that there is a negative correlation, assuming alteration of initial composition linked to biodegradation or photooxidation of humic components. Although we cannot interpret this result in terms of biogeochemical pathways of DOM transformation, it clearly indicates the high potential of DOM research in various aspects of geocryology, including both paleoclimate reconstruction and relic carbon storage/mobilization.

Figure 11. Pair scatter plot of the PARAFAC components P2 and P3.

6. Conclusions

In this research, we introduced geochemical data from ground ice observed on the Faddeevsky eastern coast (East Siberian Arctic). The distinction between ice wedges formed in the Late Pleistocene (MIS 3) and in the Holocene (MIS 1) is evident based on $\delta^{18}O$ depletion (6‰ less), lower d-excess, as well as a CH_4 fractionated hydrocarbon gas (HCG) composition due to the methane removal required for oxidation. High d-excess (11–13‰) in the Holocene IWs may be associated with the increased impact of the Atlantic and the long-range transport of air masses on the Holocene snow cover. Temperature estimates show severe winter conditions in MIS 3 during the formation of the Yedoma IC, with a mean January air temperature of $-45 \pm 3\,°C$, while in the Holocene, it was around $-35 \pm 3\,°C$. This is comparable with modern values.

The predominance of Cl^-, Na^+, and $ssSO_4^{2-}$ in TDS composition of the Holocene IW confirms the major contribution of sea-salt aerosols and proximity to the sea during the IW growth. The estimated non-sea-salt component of SO_4^{2-} ($nssSO_4^{2-}$) enrichment of the Late Pleistocene IW is most likely associated with mineral leaching of deposits under continental conditions of sea regression. Remarkably, higher DOC concentrations in the Late Pleistocene IW may indicate more favorable vegetation conditions despite the lowest winter temperatures during the proposed ice wedge growth or lower degree of organic matter

mineralization. Low DOC concentrations in the Holocene IWs and TGI are associated with limited carbon inputs or higher loss of organic matter through mineralization.

CH_4 mixing ratios in ice wedges are much higher than the atmospheric value, mainly suggesting microbial methane production prior to their occlusion in IWs or under cryogenic conditions within the ice body. Our data may indicate various environments of the methane cycle in the ice wedges of Faddeevsky, which are linked either to methane oxidation/fractionation in the Late Pleistocene IW or to methane generation/enrichment in some Holocene IWs. In comparison with our data from the Yamal Peninsula, we observe a lower degree of organic matter mineralization in more severe climate conditions of Kotelny Island.

In this study we attempted for the first time in paleoenvironmental research to use the variations in the ground ice fluorescent DOM composition to find changes in paleoclimate conditions which critically affected the features of the source water. Thus, each PARAFAC component (P1, P2, P3, P4) might represent a specific pool of DOM assigned to its biogenic producer or to a secondary process caused by initial DOM transformation before being incorporated into the ground ice. All the deconvoluted fluorophores exhibited spectral characteristics similar to those described in previous studies [54–56], supporting the existence of the common sources of DOM across latitudes. The enrichment of the P4 component, relevant to strictly autochthonous DOM in TGI, as well as high content of NH_4^+ and DIN in TGI samples, may be a feature of epigenetic freezing, conserving the environment with abundant microbial life with unrestricted nutrient availability. The humic component P2 was correlated with both DOC content and ions of the terrestrial group (Mg^{2+}, Ca^{2+}, K^+), indicating the predominantly terrestrial origin of DOC. The resulting distribution pattern of the P2–P3 ratio clearly illustrated that the DOM signatures tracked the variability in both paleoclimate conditions of the IW formation (discriminating Holocene and Pleistocene IWs) and types of ground ice (IW and TGI). This indicates the high potential of fluorescent DOM composition for tracking the paleoenvironmental conditions of ground ice formation.

In conclusion, the obtained results have refined the paleoenvironmental conditions of the Faddeevsky Peninsula in the Late Pleistocene–Holocene and, furthermore, can be applied in the differentiation of a carbon pool into fractions with different behavior in ecosystems, which is especially relevant considering the permafrost degradation in the Arctic.

References

1. Liljedahl, A.K.; Boike, J.; Daanen, R.P.; Fedorov, A.N.; Frost, G.V.; Grosse, G.; Hinzman, L.D.; Iijma, Y.; Jorgenson, J.C.; Matveyeva, N.; et al. Pan-Arctic ice-wedge degradation in warming permafrost and its influence on tundra hydrology. *Nat. Geosci.* **2016**, *9*, 312–318. [CrossRef]
2. Schuur, E.A.G.; McGuire, A.D.; Schädel, C.; Grosse, G.; Harden, J.W.; Hayes, D.J.; Hugelius, G.; Koven, C.D.; Kuhry, P.; Lawrence, D.M.; et al. Climate change and the permafrost carbon feedback. *Nature* **2015**, *520*, 171–179. [CrossRef] [PubMed]
3. Schirrmeister, L.; Kunitsky, V.; Grosse, G.; Wetterich, S.; Meyer, H.; Schwamborn, G.; Babiy, O.; Derevyagin, A.; Siegert, C. Sedimentary characteristics and origin of the Late Pleistocene Ice Complex on north-east Siberian Arctic coastal lowlands and islands—A review. *Quatern. Intern.* **2011**, *241*, 3–25. [CrossRef]
4. Streletskaya, I.D.; Pismeniuk, A.A.; Vasiliev, A.A.; Gusev, E.A.; Oblogov, G.E.; Zadorozhnaya, N.A. The ice-rich permafrost sequences as a paleoenvironmental archive for the Kara Sea region (Western Arctic). *Front. Earth Sci.* **2021**, *9*, 723382. [CrossRef]
5. Meyer, H.; Dereviagin, A.Y.; Siegert, C.; Schirrmeister, L.; Hubberten, H.W. Paleoclimate reconstruction on Big Lyakhovsky Island, North Siberia—Hydrogen and oxygen isotopes in ice wedges. *Permafr. Periglac. Process.* **2002**, *13*, 91–105. [CrossRef]
6. Vasil'chuk, Y.K. *Oxygen Isotope Composition of Ground Ice Application to Paleogeocryological Reconstructions*; Theoretical Problems Department, Russian Academy of Sciences and Lomonosov's Moscow University Publ.: Moscow, Russia, 1992; p. 420.
7. Streletskaya, I.D.; Vasiliev, A.A.; Oblogov, G.E.; Tokarev, I.V. Reconstruction of paleoclimate of Russian Arctic in Late Pleistocene–Holocene on the basis of isotope study of ice wedges. *Kriosf. Zemli* **2015**, *19*, 86–94.
8. Opel, T.; Meyer, H.; Wetterich, S.; Laepple, T.; Dereviagin, A.; Murton, J. Ice wedges as archives of winter paleoclimate: A review. *Permafr. Periglac. Process.* **2018**, *29*, 199–209. [CrossRef]
9. Porter, T.J.; Opel, T. Recent advances in paleoclimatological studies of Arctic wedge- and pore-ice stable-water isotope records. *Permafr. Periglac. Process.* **2020**, *31*, 429–441. [CrossRef]
10. Savoskul, O.S. Ion Content of polygonal wedge ice on Bolshoi Lyakhov: A source of palaeoenvironmental information. *Ann. Glaciol.* **1995**, *21*, 394–398. [CrossRef]
11. Iizuka, Y.; Miyamoto, C.; Matoba, S.; Iwahana, G.; Horiuchi, K.; Takahashi, Y.; Ohno, H. Ion concentrations in ice wedges: An innovative approach to reconstruct past climate variability. *Earth Planet. Sci. Lett.* **2019**, *515*, 58–66. [CrossRef]
12. Campbell-Heaton, K.; Lacelle, D.; Fisher, D.; Pollard, W. Holocene ice wedge formation in the Eureka Sound Lowlands, high Arctic Canada. *Quat. Res.* **2021**, *102*, 175–187. [CrossRef]
13. Streletskaya, I.D.; Vasiliev, A.A.; Oblogov, G.E.; Streletskiy, D.A. Methane content in ground ice and sediments of the Kara Sea coast. *Geosciences* **2018**, *8*, 434. [CrossRef]
14. Semenov, P.B.; Pismeniuk, A.A.; Malyshev, S.A.; Leibman, M.O.; Streletskaya, I.D.; Shatrova, E.V.; Kizyakov, A.I.; Vanshtein, B.G. Methane and dissolved organic matter in the ground ice samples from Central Yamal: Implications to biogeochemical cycling and greenhouse gas emission. *Geosciences* **2020**, *10*, 450. [CrossRef]
15. Brouchkov, A.; Fukuda, M. Preliminary measurements on methane content in permafrost, Central Yakutia, and some experimental data. *Permafr. Periglac. Process.* **2002**, *13*, 187–197. [CrossRef]
16. Boereboom, T.; Samyn, D.; Meyer, H.; Tison, J.-L. Stable isotope and gas properties of two climatically contrasting (Pleistocene and Holocene) ice wedges from Cape Mamontov Klyk, Laptev Sea, northern Siberia. *Cryosphere* **2013**, *7*, 31–46. [CrossRef]
17. Kim, K.; Yang, J.-W.; Yoon, H.; Byun, E.; Fedorov, A.; Ryu, Y.; Ahn, J. Greenhouse gas formation in ice wedges at Cyuie, central Yakutia. *Permafrost Periglac. Process.* **2019**, *30*, 48–57. [CrossRef]
18. Fellman, J.B.; Hood, E.; D'Amore, D.V.; Edwards, R.T.; White, D. Seasonal changes in the chemical quality and biodegradability of dissolved organic matter exported from soils to streams in coastal temperate rainforest watersheds. *Biogeochemistry* **2009**, *95*, 277–293. [CrossRef]
19. Stedmon, C.A.; Cory, R.M. Biological origins and fate of fluorescent dissolved organic matter in aquatic environments. In *Aquatic Organic Matter Fluorescence*; Coble, P.G., Lead, J.R., Eds.; Cambridge University Press: Cambridge, NY, USA, 2014; pp. 278–300.
20. Kellerman, A.M.; Hawkings, J.R.; Wadham, J.L.; Kohler, T.J.; Stibal, M.; Grater, E.; Marshall, M.; Hatton, J.E.; Beaton, A.; Spencer, R.G.M. Glacier outflow dissolved organic matter as a window into seasonally changing carbon sources: Leverett Glacier, Greenland. *JGR Biogeosci.* **2020**, *125*, e2019JG005161. [CrossRef]
21. Vonk, J.E.; Mann, P.J.; Davydov, S.; Davydova, A.; Spencer, R.G.M.; Schade, J.; Sobczak, W.V.; Zimov, N.; Zimov, S.; Bulygina, E.; et al. High biolability of ancient permafrost carbon upon thaw. *Geophys. Res. Lett.* **2013**, *40*, 2689–2693. [CrossRef]
22. Dubnick, A.; Sharp, M.; Barker, J.; Wadham, J.L.; Lis, G.P.; Telling, J.; Fitzsimmons, S.; Jackson, M. Characterization of dissolved organic matter (DOM) from glacial environments using total fluorescence spectroscopy and parallel factor analysis. *Ann. Glaciol.* **2010**, *51*, 111–122. [CrossRef]
23. Tumskoy, V.; Kuznetsova, T.V. Cryolithostratigraphy of the Middle Pleistocene to Holocene Deposits in the Dmitry Laptev Strait, Northern Yakutia. *Front. Earth Sci.* **2022**, *10*, 789421. [CrossRef]
24. Tumskoy, V.E. Peculiarities of cryolithogenesis in Northern Yakutia (Middle Neopleistocene to Holocene). *Kriosf. Zemli* **2012**, *16*, 12–21.
25. Vasil'chuk, Y.K.; Makeev, V.M.; Maslakov, A.A.; Budantseva, N.A.; Vasil'chuk, A.K. Late Pleistocene and Early Holocene winter air temperatures in Kotelny Island: Reconstructions using stable isotopes of ice wedges. *Kriosf. Zemli* **2019**, *23*, 13–28. [CrossRef]
26. Schirrmeister, L.; Grosse, G.; Kunitsky, V.V.; Fuchs, M.C.; Krbetschek, M.; Andreev, A.; Herzschuh, U.; Barbyi, O.; Siegert, C.; Meyer, H.; et al. The mystery of Bunge Land (New Siberian Archipelago): Implications for its formation based on palaeoenvironmental records, geomorphology, and remote sensing. *Quat. Sci. Rev.* **2009**, *29*, 3598–3616. [CrossRef]

27. Gasanov, S.S. *Cryolithological Analysis*; Nauka: Moscow, Russia, 1981; p. 196.
28. Pavlova, E.Y.; Anisimov, M.A.; Dorozhkina, M.V.; Pitulko, V.V. The tracks of old glaciation on the Novaya Sibir Island (New Siberian Islands) and it natural conditions at the Late Pleistocene. *Ice Snow* **2010**, *110*, 85–92.
29. Ivanova, V.V. Geochemical features of formation of massive ground ice bodies (New Siberia Islands, Siberian Arctic) as the evidence of their genesis. *Kriosf. Zemli* **2012**, *6*, 56–70.
30. Anisimov, M.A.; Tumskoy, V.E.; Ivanova, V.V. The subsurface ice at Novosibirskie Islands as a relic of ancient glaciation. *Mater. Glaciol. Res.* **2006**, *101*, 143–145.
31. Basilyan, A.E.; Nikolskiy, P.A.; Maksimov, F.E.; Kuznetsov, V.Y. Age of cover glaciation of the New Siberian Islands based on 230Th/U-dating of mollusk shells. In *The Structure and History of the Development of the Lithosphere*; Paulsen: Moscow, Russia, 2010; pp. 506–514.
32. Romanenko, F.A.; Nikolaev, V.I.; Arkhipov, V.V. Changes in the isotopic composition of natural ice in the East Siberian Sea: A geographical aspect. *Ice Snow* **2011**, *113*, 93–104.
33. Wetterich, S.; Meyer, H.; Fritz, M.; Mollenhauer, G.; Rethemeyer, J.; Kizyakov, A.I.; Schirrmeister, L.; Opel, T. Northeast Siberian permafrost ice-wedge stable isotopes depict pronounced Last Glacial Maximum winter cooling. *Geophys. Res. Lett.* **2021**, *48*, e2020GL092087. [CrossRef]
34. Vasil'chuk, Y.K.; Makeev, V.M.; Maslakov, A.A.; Budantseva, N.A.; Vasil'chuk, A.C.; Chizhova, J.N. The oxygen isotope composition of Late Pleistocene and Holocene ice wedges of Kotelny Island. *Dokl. Earth Sci.* **2018**, *482*, 1216–1220. [CrossRef]
35. Trufanov, G.V.; Belousov, K.N.; Vakulenko, A.S. Materials to stratigraphy of Cenozoic deposits of New Siberian Archipelago. In *Tertiary Continental Strata of the North-East of Asia*; Baranova, Y.P., Shilo, N.A., Eds.; Nauka: Novosibirsk, Russia, 1979; pp. 30–40.
36. Alekseev, M.N.; Drushchits, V.A. Climatic events of the Kazantsevo interglacial and Holocene of the Eastern part of the Russian shelf and Siberia. *BKIChP* **2001**, *64*, 78–88.
37. Pismeniuk, A.A.; Streletskaya, I.D.; Kozachek, A.V.; Malyshev, S.A.; Semenov, P.B.; Yarzhembovsky, Y.D. Ground ice of the coast of the East Siberian Sea: New data on its origin and paleoenvironmental conditions. In Proceedings of the All-Russian Conference with International Participation: The Global Problems of the Arctic and Antarctic, Arkhangelsk, Russia, 3–5 November 2020; pp. 139–143.
38. Pavlova, E.Y.; Ivanova, V.V.; Meyer, H.; Pitulko, V.V. The oxygen isotope composition of fossil ice as a climate proxy: Case study of the northern New Siberian Islands and the western Yana-Indigirka lowland. In Proceedings of the IX All-Russian Conf. on the Quaternary, V.B. Sochava Institute of Geography, Irkutsk, Russia, 15–20 September 2015; pp. 349–351.
39. Bassinot, F.C.; Labeyrie, L.L.; Vincent, E.; Quidelleur, X.; Shackleton, N.J.; Lancelot, Y. The astronomical theory of climate and the age of the Brunhes-Matuyama magnetic reversal. *Earth Planet. Sci. Lett.* **1994**, *126*, 91–108. [CrossRef]
40. Porter, C.; Morin, P.; Howat, I.; Noh, M.-J.; Bates, B.; Peterman, K.; Keesey, S.; Schlenk, M.; Gardiner, J.; Tomko, K.; et al. ArcticDEM, Version 3, Harvard Dataverse, V1. Available online: https://doi.org/10.7910/DVN/OHHUKH (accessed on 10 November 2022).
41. Veremeeva, A.; Nitze, I.; Günther, F.; Grosse, G.; Rivkina, E. Geomorphological and climatic drivers of thermokarst lake area increase trend (1999–2018) in the Kolyma Lowland Yedoma region, North-Eastern Siberia. *Remote Sens.* **2021**, *13*, 178. [CrossRef]
42. Yamamoto, S.; Alcauskas, J.B.; Crozier, T.E. Solubility of methane in distilled water and seawater. *J. Chem. Eng.* **1976**, *21*, 78–80. [CrossRef]
43. Abrams, M.A. Significance of hydrocarbon seepage relative to sub-surface petroleum generation and entrapment. *Mar. Petrol. Geol.* **2005**, *22*, 457–478. [CrossRef]
44. Trivittayasil, V.; Tsuta, M.; Kokawa, M.; Yoshimura, M.; Sugiyama, J.; Fujita, K.; Shibata, M. Method of determining the optimal dilution ratio for fluorescence fingerprint of food constituents. *Biosci. Biotechnol. Biochem.* **2015**, *79*, 652–657. [CrossRef]
45. McKnight, D.M.; Boyer, E.W.; Westerhoff, P.K.; Doran, P.T.; Kulbe, T.; Andersen, D.T. Spectrofluorometric characterization of aquatic fulvic acids for determination of precursor organic material and general structural properties. *Limnol. Oceanogr.* **2001**, *46*, 38–48. [CrossRef]
46. Stedmon, C.A.; Bro, R. Characterizing dissolved organic matter fluorescence with parallel factor analysis: A tutorial. *Limnol. Oceanogr. Methods* **2008**, *6*, 572–579. [CrossRef]
47. Murphy, K.R.; Butler, K.D.; Spencer, R.G.M.; Stedmon, C.A.; Boehme, J.R.; Aiken, G.R. Measurement of dissolved organic matter fluorescence in aquatic environments: An interlaboratory comparison. *Environ. Sci. Technol.* **2010**, *24*, 9405–9412. [CrossRef]
48. Bro, R. PARAFAC. Tutorial and applications. *Chemometr. Intell. Lab. Syst.* **1997**, *38*, 149–171. [CrossRef]
49. He, W.; Hur, J. Conservative behavior of fluorescence EEM-PARAFAC components in resin fractionation processes and its applicability for characterizing dissolved organic matter. *Water Res.* **2015**, *83*, 217–226. [CrossRef]
50. Parr, T.B.; Ohno, T.; Cronan, C.S.; Simon, K.S. comPARAFAC: A library and tools for rapid and quantitative comparison of dissolved organic matter components resolved by Parallel Factor Analysis. *Limnol. Oceanogr.-Meth.* **2014**, *12*, 114–125. [CrossRef]
51. Wetterich, S.; Tumskoy, V.; Rudaya, N.; Andreev, A.; Opel, T.; Meyer, H.; Schirrmeister, L.; Hüls, M. Ice Complex formation in arctic East Siberia during the MIS3 Interstadial. *Quatern. Sci. Rev.* **2014**, *84*, 39–55. [CrossRef]
52. Wetterich, S.; Tumskoy, V.; Rudaya, N.; Kuznetsov, V.; Maksimov, F.; Opel, T.; Meyer, H.; Andreev, A.A.; Schirrmeister, L. Ice Complex permafrost of MIS5 age in the Dmitry Laptev Strait coastal region (East Siberian Arctic). *Quatern. Sci. Rev.* **2016**, *147*, 298–311. [CrossRef]
53. Fritz, M.; Opel, T.; Tanski, G.; Herzschuh, U.; Meyer, H.; Eulenburg, A.; Lantuit, H. Dissolved organic carbon (DOC) in Arctic ground ice. *Cryosphere* **2015**, *9*, 737–752. [CrossRef]

54. Singh, S.; Inamdar, S.; Scott, D. Comparison of two PARAFAC models of dissolved organic matter fluorescence for a Mid-Atlantic forested watershed in the USA. *J. Ecosyst.* **2013**, *2013*, 532424. [CrossRef]

55. Yamashita, Y.; Cory, R.M.; Nishioka, J.; Kuma, K.; Tanoue, E.; Jaffe, R. Fluorescence characteristics of dissolved organic matter in the deep waters of the Okhotsk Sea and the northwestern North Pacific Ocean. *Deep Sea Res. Part II Top. Stud. Oceanogr.* **2010**, *57*, 1478–1485. [CrossRef]

56. Holbrook, R.D.; Yen, J.H.; Grizzard, T.J. Characterizing natural organic material from the Occoquan Watershed (Northern Virginia, US) using fluorescence spectroscopy and PARAFAC. *Sci. Total Environ.* **2006**, *361*, 249–266. [CrossRef] [PubMed]

57. Coble, P.G.; Green, S.; Blough, N.V.; Gagosian, R.B. Characterization of dissolved organic matter in the Black Sea by fluorescence spectroscopy. *Nature* **1990**, *348*, 432–435. [CrossRef]

58. Wetterich, S.; Kizyakov, A.; Fritz, M.; Wolter, J.; Mollenhauer, G.; Meyer, H.; Fuchs, M.; Aksenov, A.; Matthes, H.; Schirrmeister, L.; et al. The cryostratigraphy of the Yedoma cliff of Sobo-Sise Island (Lena delta) reveals permafrost dynamics in the central Laptev Sea coastal region during the last 52 kyr. *Cryosphere* **2020**, *14*, 4525–4551. [CrossRef]

59. Domine, F.; Sparapani, R.; Ianniello, A.; Beine, H.J. The origin of sea salt in snow on Arctic Sea ice and in coastal regions. *Atmos. Chem. Phys.* **2004**, *4*, 2259–2271. [CrossRef]

60. Vasil'chuk, Y.K. Geochemical composition of underground ice in the north of the Russian Arctic. *Arkt. Antarkt.* **2016**, *2*, 99–115. [CrossRef]

61. Patris, N.; Delmas, R.J.; Legrand, M.; Angelis, M.D.; Ferron, F.A.; Stiévenard, M.; Jouzel, J. First sulfur isotope measurements in central Greenland ice cores along the preindustrial and industrial periods. *J. Geophys. Res. Atmos.* **2002**, *107*, ACH 6-1–ACH 6-11. [CrossRef]

62. Leck, C.; Persson, C. The central Arctic Ocean as a source of dimethyl sulfide Seasonal variability in relation to biological activity. *Tellus B Chem. Phys. Meteorol.* **1996**, *48*, 156–177. [CrossRef]

63. Jones, E.L.; Hodson, A.J.; Thornton, S.F.; Redeker, K.R.; Rogers, J.; Wynn, P.M.; Dixon, T.J.; Bottrell, S.H.; O'Neill, H.B. Biogeochemical processes in the active layer and permafrost of a High Arctic fjord valley. *Front. Earth Sci.* **2020**, *8*, 342. [CrossRef]

64. Holland, K.M.; Porter, T.J.; Criscitiello, A.S.; Froese, D.G.; Kokelj, S. Marine aerosol contribution to ice-wedge geochemistry: Potential for paleo-sea ice and paleogeography reconstructions in the Canadian Arctic. In Proceedings of the AGU Fall Meeting, Online, 1–17 December 2020.

65. Schüpbach, S.; Fischer, H.; Bigler, M.; Erhardt, T.; Gfeller, G.; Leuenberger, D.; Stowasser, O.; Mulvaney, R.; Abram, N.; Fleet, L.; et al. Greenland records of aerosol source and atmospheric lifetime changes from the Eemian to the Holocene. *Nat. Commun.* **2018**, *9*, 1476. [CrossRef] [PubMed]

66. Wynn, P.M.; Hodson, A.J.; Heaton, T.H.E.; Chenery, S.R. Nitrate production beneath a High Arctic glacier, Svalbard. *Chem. Geol.* **2007**, *244*, 88–102. [CrossRef]

67. Makeev, V.M.; Arslanov, K.A.; Baranovskaya, O.F.; Kosmodamiansky, D.P.; Tertychnaya, T.V. Late Pleistocene and Holocene stratigraphy, geochronology, and paleogeography of Kotelny Island. *Bull. Quat. Comm.* **1989**, *58*, 58–69.

68. Yang, Y.; Guo, X.; Wang, Q.; Jin, H.; Yun, H.; Wu, Q. Dissolved organic carbon (DOC) in ground ice on northeastern Tibetan Plateau. *Front. Earth Sci.* **2022**, *10*, 782013. [CrossRef]

69. Spencer, R.G.M.; Mann, P.J.; Dittmar, T.; Eglinton, T.I.; McIntyre, C.; Holmes, R.M.; Zimov, N.; Stubbins, A. Detecting the signature of permafrost thaw in Arctic rivers. *Geophys. Res. Lett.* **2015**, *42*, 2830–2835. [CrossRef]

70. Guo, L.; Ping, C.-L.; Macdonald, R.W. Mobilization pathways of organic carbon from permafrost to arctic rivers in a changing climate. *Geophys. Res. Lett.* **2007**, *34*, L13603. [CrossRef]

71. Whiticar, M.J. Carbon and hydrogen isotope systematics of bacterial formation and oxidation of methane. *Chem. Geol.* **1999**, *161*, 291–314. [CrossRef]

72. Rivkina, E.; Petrovskaya, L.; Vishnivetskaya, T.; Krivushin, K.; Shmakova, L.; Tutukina, M.; Meyers, A.; Kondrashov, F. Metagenomic analyses of the late Pleistocene permafrost—Additional tools for reconstruction of environmental conditions. *Biogeosciences* **2016**, *13*, 2207–2219. [CrossRef]